Interdecadal Variations in ENSO Teleconnection to the Indo–Western Pacific for 1870–2007*

J. S. Chowdary,[+,#] Shang-Ping Xie,[+,@,&] Hiroki Tokinaga,[+] Yuko M. Okumura,[+,**] Hisayuki Kubota,[++] Nat Johnson,[+] and Xiao-Tong Zheng[&]

[+] *International Pacific Research Center, University of Hawaii at Manoa, Honolulu, Hawaii*
[#] *Indian Institute of Tropical Meteorology, Pune, India*
[@] *Department of Meteorology, University of Hawaii at Manoa, Honolulu, Hawaii*
[&] *Physical Oceanography Laboratory, Ocean University of China, Qingdao, China*
[**] *National Center for Atmospheric Research, Boulder, Colorado*
[++] *Japan Agency for Marine-Earth Science and Technology, Yokosuka, Japan*

ABSTRACT

Slow modulation of interannual variability and its relationship to El Niño–Southern Oscillation (ENSO) is investigated for the period of 1870–2007 using shipboard surface meteorological observations along a frequently traveled track across the north Indian Ocean (NIO; from the Gulf of Aden through Malacca Strait) and the South China Sea (to Luzon Strait). During the decades in the late nineteenth–early twentieth century and in the late twentieth century, the El Niño–induced NIO warming persists longer than during the 1910s–mid-1970s, well into the summer following the peak of El Niño. During the epochs of the prolonged NIO warming, rainfall drops and sea level pressure rises over the tropical northwest Pacific in summer following El Niño. Conversely, during the period when the NIO warming dissipates earlier, these atmospheric anomalies are not well developed. This supports the Indian Ocean capacitor concept as a mechanism prolonging El Niño influence into summer through the persistent Indian Ocean warming after El Niño itself has dissipated.

The above centennial modulation of ENSO teleconnection to the Indo–northwest Pacific region is reproduced in an atmospheric general circulation model forced by observed SST. The modulation is correlated not with the Pacific decadal oscillation but rather with the ENSO variance itself. When ENSO is strong, its effect in the Indo–northwest Pacific strengthens and vice versa. The fact that enhanced ENSO teleconnections occurred 100 years ago during the late nineteenth–early twentieth century indicates that the recent strengthening of the ENSO correlation over the Indo–western Pacific may not entirely be due to global warming but reflect natural variability.

1. Introduction

El Niño–Southern Oscillation (ENSO) is the dominant mode of climate variability in the instrumental record, affecting climate around the globe via atmospheric teleconnections. ENSO teleconnections are the basis for seasonal prediction and have been studied extensively.

With the accumulation of observations, evidence is emerging that some ENSO teleconnections, for example, for summer climate over India (Kumar et al. 1999) and the Indo–western Pacific (Xie et al. 2010; Huang et al. 2010), are not stable in time but experience substantial interdecadal modulations. Many studies of such low-frequency modulations of interannual variability are limited to recent decades after 1950 (Nitta and Yamada 1989; Trenberth and Hurrell 1994; Terray and Dominiak 2005; Annamalai et al. 2005; Xie et al. 2010), owing to the lack of high-quality observations over tropical oceans.

A few studies have examined ENSO-induced SST variability over the Indo–western Pacific region prior to World War II. Allan et al. (1995) studied the mean conditions over the Indian Ocean region during four 21-yr epochs since 1900 and suggested that epochal change is in phase

Corresponding author address: J. S. Chowdary, International Pacific Research Center, University of Hawaii at Manoa, Honolulu, HI 96822.
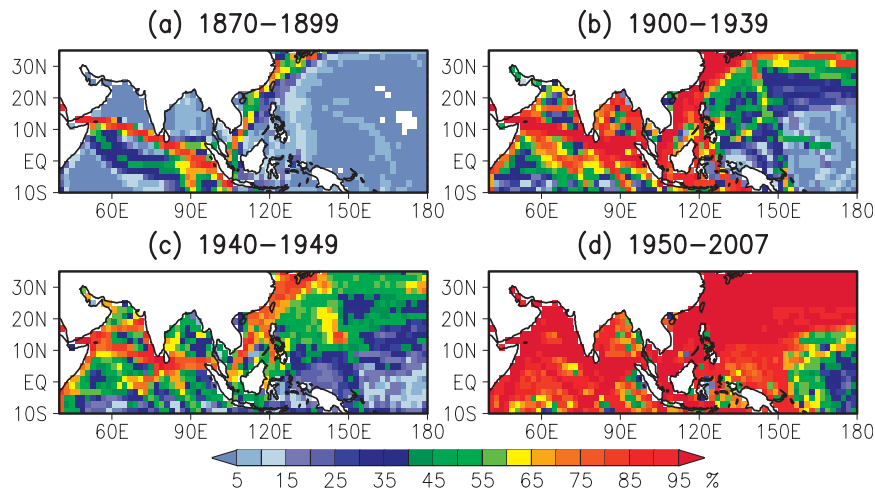E-mail: sriranga@hawaii.edu

FIG. 1. Distribution of sea surface temperature observations from the ICOADS for (a) 1870–99, (b) 1900–39 (before World War II), (c) 1940–49 (during and shortly after World Wars), and (d) 1950–2007 (after World War II). Color shading indicates the percentage of months with at least one measurement in a 2° × 2° longitude and latitudinal box.

with ENSO-related correlation pattern. Their study focuses mainly on the south Indian Ocean during the mature phase of El Niño. Using composites of pronounced ENSO events from the late nineteenth century to 1989, Reason et al. (2000) examined anomalies of SST, mean sea level pressure, and cloudiness over the Indian Ocean. Allan et al. (2003) studied interference of variability on quasi-biennial to quasi-decadal time scales for 1870 to 2000 in forming "protracted" ENSO episodes and affecting climate around the Indian Ocean rim.

This study examines interdecadal modulation of ENSO teleconnections into the Indo–western Pacific during the period 1870–2007, which has not been systematically studied in the literature. In particular, the present study overcomes the limitation of sparse high-quality data before 1950s with the use of observations along frequently traveled shipping lanes to examine long-term variations in ENSO teleconnections. Specifically, the opening of the Suez Canal in 1869 substantially shortened shipping routes from Europe to East Asia, channeling the traffic along a narrow track across the north Indian Ocean (NIO) from the tip of the African horn through the Malacca Strait and across the South China Sea to the Luzon Strait. In general, surface meteorological observations are well sampled along this busy shipping lane (Fig. 1), offering a rare opportunity to study interannual variability over NIO/South China Sea for more than 100 years since 1870. Hereafter, we denote seasons during the developing and decay years of El Niño with (0) and (1), respectively. Seasons are defined by those of the Northern Hemisphere.

The tropical Pacific exerts strong influence over tropical Indian Ocean variability during and after the mature

phase of El Niño via teleconnections (Allan et al. 1995; Klein et al. 1999; Reason et al. 2000; Alexander et al. 2002; Kinter et al. 2002; Shinoda et al. 2004; Ashok et al. 2007; Schott et al. 2009; Du et al. 2009; Xie et al. 2009, 2010). The tropical Indian Ocean basinwide warming, induced by El Niño at its mature phase, proves to have important effects on the atmospheric circulation elsewhere. Previous studies have shown that the tropical Indian Ocean sea surface temperature (SST) anomalies induce significant changes in the atmospheric circulation over the Northern Hemisphere (e.g., Watanabe and Jin 2002; Annamalai et al. 2005, 2007). Basinwide warming as a "capacitor" persists from spring to summer after the mature phase of ENSO and substantially impacts atmospheric circulation over South Asia (Yang et al. 2007). The persistent tropical Indian Ocean warming also exerts influence on northwest Pacific climate during summer after El Niño {June–August [JJA](1)} through the Kelvin wave–induced Ekman divergence mechanism–capacitor effect (Xie et al. 2009), described as follows. In response to the tropical Indian Ocean warming during JJA(1), tropospheric temperature anomalies display a Matsuno (1966)–Gill (1980) pattern. A warm Kelvin wave in tropospheric temperature propagates into the equatorial western Pacific, inducing northeasterly surface wind anomalies on the northern flank of the Kelvin wave. The surface friction–induced subtropical divergence suppresses convection over the northwest Pacific, and the resulting feedback between convection and circulation gives rise to an anomalous anticyclone in the lower troposphere. Chowdary et al. (2011) test this Kelvin wave–induced Ekman divergence mechanism with forecast model

experiments. By decoupling the tropical Indian Ocean variability, their study finds that without tropical Indian Ocean influence, the northwest Pacific atmospheric anomalies weaken by 50% in JJA(1).

Recent studies point to the strengthening of ENSO teleconnections to the northwest Pacific in JJA(1) (B. Wang et al. 2008) as evidenced in tropical Indian Ocean SST after the 1970s (Xie et al. 2010). The latter study suggests that a slowly decaying El Niño induces a more robust and persistent response over the tropical Indian Ocean and northwest Pacific after the 1970s regime shift. Furthermore, Xie et al. (2010) show that through the mechanism of Kelvin wave–induced Ekman divergence, a strong tropical Indian Ocean response translates into a pronounced development of atmospheric anomalies over the northwest Pacific in JJA(1) after the 1976/77 regime shift. As the tropical Indian Ocean SST warming does not persist through JJA(1) before the 1976/77s, atmospheric anomalies over the northwest Pacific weaken and are not well organized in space. Epochal changes in the spatiotemporal structure of the tropical Indian Ocean SST response to ENSO are also documented in their study. The SST warming over the NIO displays a peculiar double-peak structure, one at the mature phase of the El Niño and one during early summer following the El Niño peak (Du et al. 2009). An equatorially antisymmetric pattern of wind anomalies is key to the NIO warming during summer after El Niño (Du et al. 2009). Northeasterlies to the north of the equator and northwesterlies to the south, opposing the prevailing southwest monsoon mean winds, reduce surface evaporation and thereby warm the NIO. The antisymmetric wind pattern is anchored by the persistent SST warming over the southwest tropical Indian Ocean due to downwelling Rossby waves from the east (Xie et al. 2002; Du et al. 2009). This double-peak pattern in NIO warming is strong in the recent epoch after the 1970s but absent in the three decades before the 1970s (Xie et al. 2010). The second peak in NIO warming in turn plays an important role in maintaining the northwest Pacific atmospheric anomalies in JJA(1) and in reducing the frequency of tropical cyclones to the east of Philippines (Du et al. 2011). The strength of the summer northwest Pacific anticyclone is highly correlated with NIO SST (Xie et al. 2010; Huang et al. 2010).

The present study examines Indo–western Pacific climate variability in summer and its relationship with ENSO using the NIO–South China Sea ship track data and island meteorological observations dating back to late nineteenth century (1870–2007). The analysis of the historical SST is critical to our understanding of past, present, and future climate change. Following upon the recent studies of Xie et al. (2010) and Du et al. (2009),

we examine interannual and interdecadal variability over the Indo–western Pacific associated with ENSO decay phase for different epochs. A major challenge in investigating the nature of epochal change in teleconnections is the lack of long-term observed data. Most studies of interdecadal ENSO teleconnections are based on atmospheric reanalysis, which are known to suffer spurious changes across the 1970s (Wu and Xie 2003) most likely because of the substantial increase and assimilation of satellite data. Our analysis of frequently traveled ship lanes data and land–station observations show that there are strong epochal changes in the ENSO's influence on the Indo–western Pacific during JJA(1) for the period of 1870–2007. These results are supported by atmospheric model simulations forced with observed SST for the nearly 140-yr period. Our results suggest that the natural variability and in association with changes in ENSO variance is the key for epochal changes in ENSO's influence on the Indo–western Pacific.

The paper is organized as follows. The following section outlines the details of different datasets used in the study. Section 3 presents dominant modes and trends in NIO ship SST. Section 4 discusses ENSO influence on the NIO in different epochs. Underlying mechanisms responsible for epochal differences in NIO warming and air–sea interactions are outlined in section 5. Section 6 describes epochal change in ENSO teleconnections to the South China Sea and northwest Pacific climate. Section 7 provides atmospheric general circulation model (AGCM)-simulated teleconnection changes in different epochs. Section 8 discusses possible causes for change in epochal teleconnections over the Indo–western Pacific linked to ENSO. The major results and conclusions of this study are summarized in section 9.

2. Data, model, and analysis methods

Weather observations are essential for global and regional climate studies and prediction. We use frequent ship lanes surface marine data over the Indo–western Pacific region from the mouth of Gulf of Aden, through Malacca Straits and the South China Sea and the Luzon Strait to East Asia for the period of 1870–2007 (Fig. 1). Dense data along such frequent ship lanes give strong evidence for the long-term climate variability and Indo–western Pacific teleconnections to ENSO, whereas widely used gridded SSTs tend to be affected by large-scale SST variability away from targeted regions because of their spatial interpolation methods such as the empirical orthogonal functions (EOFs) (Kaplan et al. 1998; Smith et al. 1998). We apply a simple linear average along the frequently traveled ship lanes over three regions, the NIO, South China Sea, and northwest Pacific, which are
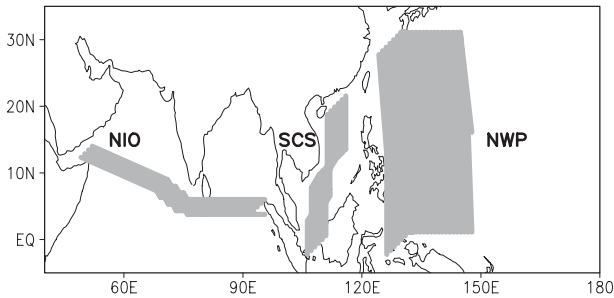
FIG. 2. Data averaged along the ship tracks (gray shading) over the NIO, South China Sea, and northwest Pacific are used for analysis during period of 1870–2007.

defined as 2° grid boxes that contain monthly mean SSTs for more than 80% of the total months from 1870 to 2007 (Fig. 2). Because the data coverage of each northwest Pacific ship lane is 50%–70% for the entire period, we average the data zonally around 130°–150°E by taking advantage of zonally uniform characteristics of ocean–atmosphere anomalies over this region.

Surface wind velocity, SST, cloudiness, specific humidity, and sea level pressure (SLP) data along ship lanes are extracted from the International Comprehensive Ocean–Atmosphere Dataset (ICOADS) 2.5 (Woodruff et al. 2011). All data have been trimmed using the ICOADS quality-control flag that identifies potential outliers based on the climatological 4.5 standard deviation limits. This is basically the same quality control as used for the enhanced product of the ICOADS Monthly Summary Groups available at the Research Data Archive (RDA) at the National Center for Atmospheric Research (NCAR). The record length of ~140 years (1870–2007) allows the investigation of the Indo–western Pacific climate variability associated with ENSO in different multidecadal epochs. Discontinuity in ship meteorological parameters is identified during World War II and a few years thereafter, which is due to the Suez Canal being closed several times during armed conflicts. This causes significant data gaps in 1940s along ship lanes. To avoid such a discontinuity in our SST analysis, we have filled the gap with Hadley Centre Global Sea Ice and Sea Surface Temperature (HadISST1) for the 1940s period. Global mean SSTs drop in the 1940s owing to differences in SST measurement techniques (Thompson et al. 2008). SST data were sampled on board ships using a variety of measurement techniques, including measurements taken from insulated and uninsulated buckets and engine room intakes (e.g., Folland and Parker 1995; Rayner et al. 2006). Corrections for the discontinuity or jumps in SST data in 1940s are expected to alter the character of midtwentieth-century temperature variability but not the estimate of the century-long trend in global-mean

temperatures (Thompson et al. 2008) and teleconnections. Our results discussed in the paper are unaffected by the sudden drop and data gap in the 1940s.

Several other SST products are used to compare with ship track SST data. We have extracted monthly SST data along the ship tracks over the Indo–western Pacific region from different SST reanalysis products. These datasets include HadISST1 on a 1° latitude–longitude grid from 1870 to date (Rayner et al. 2003), the National Oceanic and Atmospheric Administration (NOAA)–National Climatic Data Center (NCDC) Extended Reconstruction SST (ERSST) version 2 (Smith and Reynolds 2004), the extended Kaplan SST dataset (Kaplan et al. 1998) and Centennial in situ Observation-Based Estimates of SSTs (COBE-SST; Ishii et al. 2005) from the Japan Meteorological Agency (JMA).

Observed station (e.g., Seychelles) rainfall data for twentieth century is obtained from NOAA. In addition, we make use of the gridded dataset of land monthly precipitation for the 1850–1995 of Dai et al. (1997) and the Climate Prediction Center (CPC) Merged Analysis for Precipitation (CMAP; Xie and Arkin 1997). Using the distance-weighted scheme, Dai et al. (1997) interpolated historical land station precipitation data onto a 2.5° × 2.5° grid. The spatial sampling error for the gridded precipitation anomalies is large (up to 45%) for areas having only a few stations per 2.5° × 2.5° grid box. Thus signals in precipitation fields covering only a few 2.5° × 2.5° grid boxes are generally not important, especially in sparsely covered areas (Dai et al. 1997). To overcome this problem, rain gauge–based precipitation data are constructed for the Philippines and Guam for the period of 1900 to 2007. A simple linear average for 37 Philippine stations is used from the Monthly Bulletins of Philippine Weather Bureau (Kubota and Chan 2009).

In addition to the observational data described above, we analyze a five-member ensemble integration with the NCAR Community Atmosphere Model, version 3 (CAM3; Collins et al. 2006) forced by observed monthly SSTs over the tropical oceans (20°S–20°N) during 1871–2001 from the dataset of Hurrell et al. (2008). Outside the tropics, climatological monthly SSTs are prescribed, with a linear transition between 20° and 30°. The horizontal resolution of the model is T85, equivalent to 1.4° latitude 1.4° longitude. The ensemble members differ only in their initial conditions. This integration is referred as Tropical Ocean–Global Atmosphere (TOGA) simulation. The CAM3 TOGA run has been conducted by the NCAR Community Earth System Model Climate Variability Working Group and made available to the community (http://www.cesm.ucar.edu/working_groups/Variability/experiments.html). Both observational and model results are further compared with twentieth-century reanalysis

(20CR) (Compo et al. 2011). Tropospheric temperature is represented by the model geopotential height difference between 200 and 500 hPa.

Climate indices are essential for examining the interdecadal modulations in global teleconnection patterns. Therefore in this study, various climate indices are obtained from different sources. Southern Oscillation index (SOI) based on marine surface observations is used (Allan et al. 1991). The Niño-3.4 index is computed using the ICOADS 2.5 SST anomalies. Note that the density of observations in the Niño-3.4 region may differ from the NIO in late 1800s. However, we have compared our Niño-3.4 index with different datasets (e.g., HadISST1 and ER SST) and found that our Niño-3.4 index is highly correlated with other datasets. Correlation coefficient between November–January (NDJ) Niño-3.4 index and the December–February (DJF) SOI is -0.88 for epoch 1 and is -0.83 for the entire study period. The Pacific decadal oscillation (PDO; Mantua et al. 1997) and the interdecadal Pacific oscillation (IPO; Power et al. 1999) indexes are calculated from HadISST1. EOF, linear correlation, and regression analyses are used to quantify the relationship between ENSO and climate anomalies of the Indo–western Pacific region. A season-reliant EOF (S-EOF) analysis method (Kim and Wu 1999; Wang and An 2005) is used to objectively identify the ENSO-related mode in different epochs. The advantages of the S-EOF as compared to the conventional EOF analysis are described in detail in B. Wang et al. (2008). Latent heat flux (LHF), obtained from ship meteorological data, is decomposed as the oceanic response that arises from the SST dependence on evaporation (Newtonian cooling) and atmospheric forcing (AtF-L) due mostly to changes in wind speed, relative humidity, and air–sea temperature difference (de Szoeke et al. 2007; Du and Xie 2008; Du et al. 2009). Shortwave (SW) radiation is computed based on the bulk formula of Gill (1982). Monthly varying cloudiness from ship track data and clear-sky radiation from the International Satellite Cloud Climatology Project (ISCCP) are used for the SW radiation calculation. Ship data anomalies are calculated based on the monthly mean climatology for the period of 1870–2007. A 9-yr running mean is removed to suppress the decadal and long-term variations in the datasets. To reduce the effect of pronounced intraseasonal variability over the Indo–western Pacific Oceans, a 3-month running average is applied. The typical decorrelation time for such bandpass-filtered time series is slightly more than half a year. We estimate the total degree of freedom as (analysis period in years)/1.5. For a 21-yr (27-yr) time series, a correlation of 0.43 (0.38) and 0.5 (0.44) reaches the 90% and 95% significance level, respectively, based on a two-tailed Student's t test.

3. Dominant modes and trend in NIO SST

The 137-yr unfiltered monthly SST anomaly time series averaged along the NIO ship track is shown in Fig. 3a. A clear warming trend with ~1.4°C over the 137-yr period (thin dotted line) occurs in the NIO SST. The warming trend of ~0.1°C per decade is consistent with many other regional warming trends of different tropical oceans (e.g., Wang and Mehta 2008). There are interannual warming and cooling events evident in the detrended ship SST anomaly over the NIO (Fig. 3b). Bandpass-filtered NIO SST exhibits large variations with significant peaks at 1.5 and 3.5 years in the Fast Fourier Transform analysis (not shown), which are associated with ENSO. The correlation between NIO ship SST and other SST products along the ship track is high ($r > 0.8$) for the entire period of 1870–2007 (Fig. 4a), indicating a consistency with other analyzed datasets. The standard deviations of the NIO SST anomalies along the ship track are low over most of the Bay of Bengal but high over the southern tip of India and western Arabian Sea, a pattern that resembles the leading EOF pattern (Figs. 4b,c). The leading EOF explains 63.62% and 76.66% of the variance for ship track and HadISST data, respectively. The explained variance is larger for the spatial-smoothed HadISST data. High standard deviation over the southern tip of India is associated with ocean dynamics and thermodynamics during both summer and winter monsoon seasons, respectively (McCreary et al. 1993; Rao et al. 2008). The western Arabian Sea SST variability is strongly influenced by ocean dynamics such as upwelling and horizontal advection (McCreary et al. 1993; Murtugudde et al. 2000; Behera et al. 2000). Interannual variance is higher in the ship track data than in the HadISST, as the latter is heavily smoothed in space. The correlation between the leading principal components of ship data and HadISST is high over the NIO (Fig. 4d). The principal component lagged correlation with the Niño-3.4 index, where the Niño-3.4 index leads by 3 months, for both SST data exceeds 0.6 for the 137-yr period, which is highly significant at more than the 99% confidence level (Fig. 4d).

4. NIO warming associated with El Niño

El Niño–induced SST warming over the tropical Indian Ocean–NIO generally starts in [September–November (SON)] SON(0) and persists for 1–3 seasons. Figure 5 shows the correlation in 21-yr sliding windows between NIO SST averaged along the ship track and NDJ(0/1) Niño-3.4 index. Visual inspection of the correlation analysis reveals that there are four prominent epochs characterized by significantly strong warming bands. They are (i) 1883–1909 (epoch 1), (ii) 1910–36 (epoch 2), (iii)
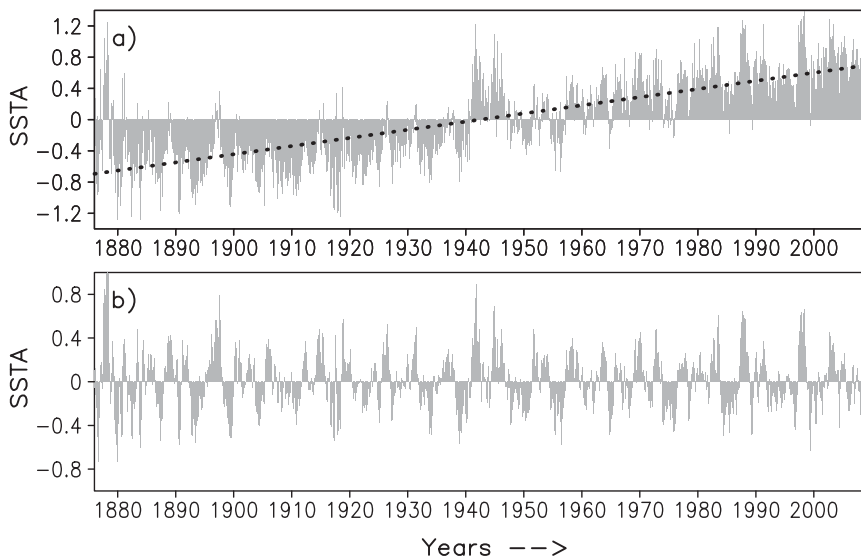
FIG. 3. (a) Time series of monthly mean SST anomaly (°C) averaged along the NIO ship track for 1870–2007 and (b) time series after removing trend. Dotted line denotes the linear trend in (a).

1950–76 (epoch 3), and (iv) 1977–2003 (epoch 4). These epochs are selected based on the seasonal shift in NIO SST warming associated with ENSO. Based on the SOI index Allan et al. (1995) studied epoch-mean anomalies over the Indian Ocean. Our aim here is to study the slow modulation of ENSO teleconnection to the Indo–western Pacific (including the north Indian Ocean). Therefore, we have considered relation between NDJ(0/1) Niño-3.4 index and NIO SST to determine the epochs. This study will not examine from the 10-yr period of 1940–49 because of poor data coverage during and immediately after World War II. Figure 5 shows that in epoch 1, NIO SST warming displays a double-peak pattern, first peaking at [October–December (OND)] OND(0) and second at early summer after the El Niño mature phase. The early decades of the twentieth century between 1910 and 1940 display a maximum correlation (warming) over the NIO in [March–May (MAM)] MAM(1). The maximum warming band shifted to NDJ(0/1) around 1950 and continued until the mid-1970s. Similar to epoch 1, epoch 4 also displays a double-peak pattern but the first peak appears in SON(0). The peak correlations are statistically significant at the 95% confidence level according to a two-tailed t test.

Figure 6 displays the correlation of SST and surface winds with the NDJ(0/1) Niño-3.4 SST index as a function of longitude and calendar month along the NIO ship track in the four different epochs. Coherent changes in SST anomalies over the NIO among the four epochs are evident across the ship track. Epoch 1 displays a large single-peak warming from SON(0) to the early following fall east of 77°E, while in the west (in the Arabian Sea)

maximum warming is seen during OND(0) and JJA(1) seasons. During epoch 2, SST warming is stronger in the Bay of Bengal (east of 77°E) with a single warming peak around MAM(1), and the Arabian Sea warming shows some signals of a weak double peak similar to that of epoch 1. Coherent single-peak structure is evident in epoch 3 with the maximum warming centered at NDJ(0/1) in most of the NIO. Warming signals in epoch 4 are more like that of epoch 1 along the NIO ship track. The winter peak in the Arabian Sea is common to all epochs, whereas the summer peak is variable in timing and magnitude. In the Bay of Bengal, the onset, peak, and decay of the SST warming vary from epoch to epoch. During epoch 1, surface northeasterly wind anomalies associated with El Niño prevail in [December–January (DJ)] DJ(0/1) over the NIO. In epoch 2, northeasterly anomalies are seen during SON(0) and MAM(1) over the Arabian Sea and in JFM(1) in the Bay of Bengal. Wind correlations are strong from June(0) to December(0) in epoch 3 during the El Niño developing year but weak after the peak phase of El Niño. In the most recent epoch, the prevailing northeasterlies are strongest from SON(0) to MAM(1) over the NIO. Surface wind variations play an important role in maintaining the SST warming over the NIO as discussed in the next section. For correlations with the SOI, all four epochs show similar patterns in NIO SST and surface winds (not shown). The most prominent feature noted in Fig. 6 is the distinct double-peak warming pattern that occurred over the Arabian Sea both in epoch 1 and in epoch 4. The second NIO warming peak in JJA(1) plays a critical role in maintaining northwest Pacific atmospheric anomalies (Xie et al. 2009) including a contribution to the
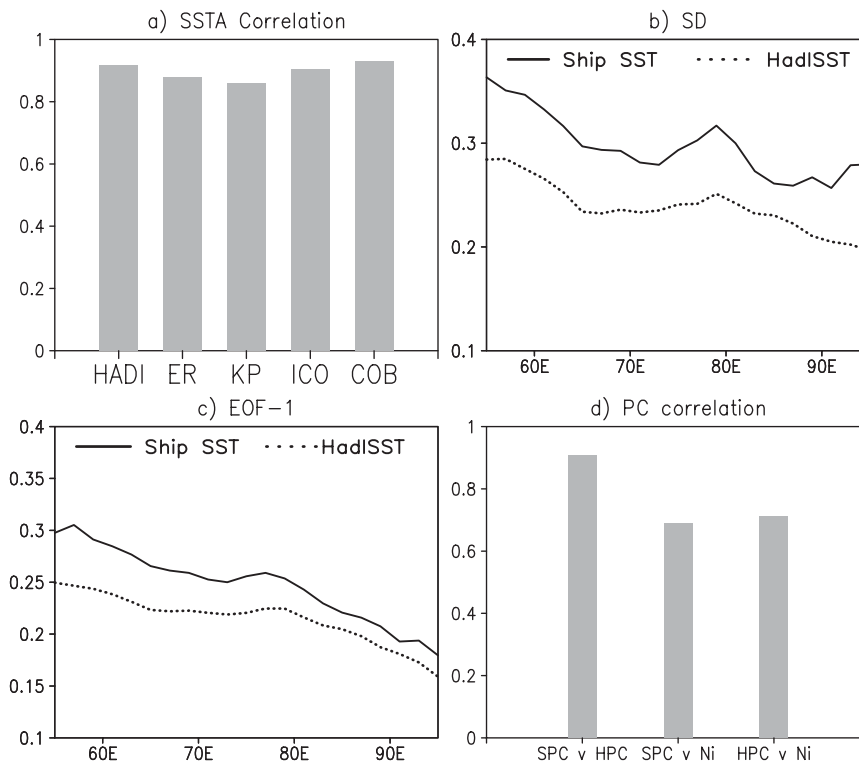
FIG. 4. (a) Correlation between ship NIO SST anomaly time series and that of different SST products (HadISST1, ERSST, Kaplan SST, ICOADS 2.0, and COBE-SST), (b) standard deviation (°C) of ship data and HadISST1 SST, (c) first EOF of NIO SST, and (d) principal component correlation between ship data (SPC) and HadISST1 (HPC) and correlation of first principal component with Niño-3.4 index, where the Niño-3.4 index led by 3 months.

reduction in the number of tropical cyclones over the Philippines Seas (Du et al. 2011). Correlation patterns are somewhat different between the Arabian Sea and Bay of Bengal (Fig. 6) but epochal differences in the Arabian Sea are similar to those for the entire NIO ship track. For example, In epoch 1 (epoch 4), for both the NIO and Arabian Sea, SST warming displays a double-peak pattern, the first peak in DJF(0/1) [OND(0)] and second in early summer after the El Niño mature phase.

Prior to examining the mechanism associated with differences in warming among four epochs, we conduct S-EOF analysis from DJF(0) (a year before the mature phase of El Niño) to DJF(2) (a year after the mature phase of El Niño) to objectively identify SST modes over the NIO. Figure 7 shows the ENSO-related S-EOF SST modes, which are very similar to the SST anomalies associated with ENSO obtained via correlation analysis. The time series of the principal component corresponding to the ENSO-related S-EOF is significantly correlated with NDJ(0/1) Niño-3.4 index, with the value of 0.76, 0.90, 0.70, and 0.75 for epochs 1, 2, 3, and 4, respectively (all above 95% confidence level). Note that in epoch 1, the second S-EOF mode of NIO SST is associated with

ENSO and for all the other epochs it is the first mode. The percentage of variance over the 27-yr record explained by these SST S-EOF modes are 26.3% (S-EOF2), 23.7%, 28.4% and 28.9% for epochs 1, 2, 3, and 4, respectively. In epoch 1 the variance contribution of S-EOF1 is 28.97%, slightly greater than that of S-EOF2 (26.3%). During this epoch correlation between the PC2 and NDJ(0/1) Niño-3.4 SST index is 0.76 whereas the correlation is 0.56 for PC1. Thus the S-EOF2 pattern for NIO SST is strongly related to ENSO. The regressions of surface wind anomalies with the corresponding SST S-EOF principal component in different epochs are also shown in Fig. 7. The wind patterns are similar to those in the correlation analysis of Fig. 6. Thus, S-EOF analysis further supports the selection of these four epochs in the current study.

5. Underlying mechanisms: Role of air–sea interactions

a. Local air–sea interactions

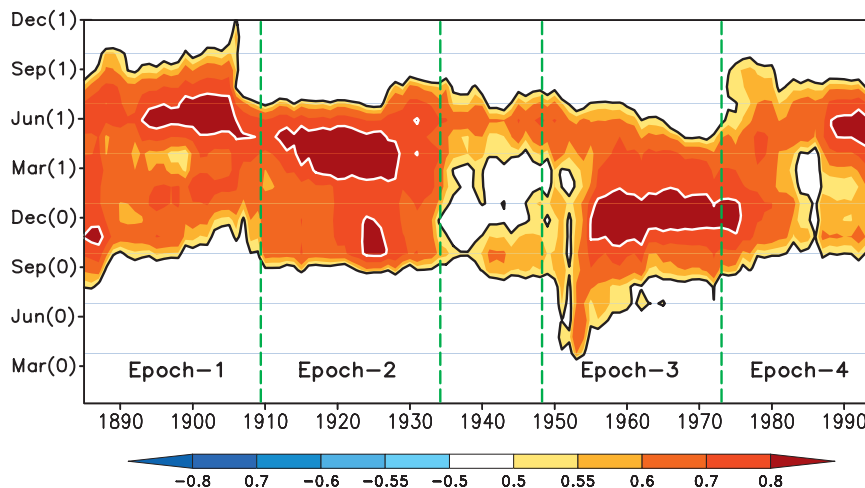The ENSO-induced large-scale atmospheric teleconnections alter the near-surface air temperature, humidity,

FIG. 5. Correlation (shaded) in 21-yr sliding windows between NIO SST anomalies (averaged along ship track) and NDJ(0/1) Niño-3.4 index. Green-dashed lines divide the data into four epochs to study the interdecadal variations associated with ENSO. Solid and black contours represent the 95% confident level, and white contours represent correlations above 0.8.

and wind, as well as the distribution of clouds over tropical Indian Ocean. The resulting variations in the surface heat, momentum, and freshwater fluxes force SST anomalies in the NIO during ENSO (Klein et al. 1999; Alexander et al. 2002; Du et al. 2009). Many studies emphasize the role of heat fluxes in this region based on observational analyses (Yu and Rienecker 1999; Reason et al. 2000; Tokinaga and Tanimoto 2004; Chowdary and Gnanaseelan 2007; Du et al. 2009) and models (Behera et al. 2000; Venzke et al. 2000).

Ship reports include observations of cloudiness, wind speed, surface air temperature and relative humidity, permitting calculation of surface heat flux along ship tracks starting from the 1870s. Figure 8 shows the regression of the atmospheric component of LHF (AtF-L), surface wind speed, and SW radiation upon the NDJ(0/1) Niño-3.4 index in all four epochs. Positive anomalies of AtF-L indicate ocean warming and negative anomalies indicates cooling. The NIO SST warming is characterized by a double-peak pattern in epoch 1 and is particularly strong in the Arabian Sea (Fig. 6). Figure 8a indicates the warming in the late spring and summer after El Niño seems to be influenced by variations in the AtF-L and SW radiation. Northeasterly wind anomalies during this period, opposing the mean southwesterlies, act to reduce the LHF and to warm the SST over the NIO. In addition to AtF-L, the increased shortwave radiation acts to increase SST over the Bay of Bengal. Warming in OND(0) (first peak) in the Arabian Sea is not well explained by heat flux. This could be due to limited surface meteorological data during epoch 1 and therefore one must consider this result with some caution. In epoch 2, the NIO

SST warming is characterized approximately by a single-band-like structure starting from SON(0) until AMJ(1). In both the Arabian Sea and Bay of Bengal, AtF-L is in phase with SST tendency in most of the period during this epoch (Figs. 6b and 8b). The reduced mean wind speed in the late summer and fall of the El Niño developing year along with large-scale ENSO-related subsidence (positive SW radiation) act to enhance SST over the NIO. In late winter and spring of the El Niño decay phase again both AtF-L and SW radiation seem to be responsible for warming in the NIO, in particular over the Arabian Sea.

In epoch 3, positive SST anomalies decay rapidly after [January–February (JF)] JF(1) in the Arabian Sea (Fig. 6c). During this epoch, AtF-L appears to be more dominant in controlling the SST than SW radiation. Warming during epoch 3 decreases rapidly compared to other epochs because of a sudden change in heat flux components (Fig. 8c). Wind speed variations are consistent with AtF-L and hence the SST pattern. Unlike other epochs, during epoch 4 northeasterly wind anomalies persist for 3–4 seasons over the NIO. Figure 8d shows that AtF-L is consistent with the double-peak SST warming pattern.

The warming associated with the first peak during SON(0) is mostly confined to the Arabian Sea where the anomalous northeasterlies weaken the mean southwesterlies (Lau and Nath 2000; Du et al. 2009), and the resulting AtF-L warms the SST there. SST cooling in the late winter and early spring is due to the AtF-L response to wind anomalies. Strong easterly wind anomalies intensify the northeast monsoon mean winds, cooling the SST owing to increased latent heat fluxes over the NIO. The asymmetric mode in wind anomalies with northeasterlies
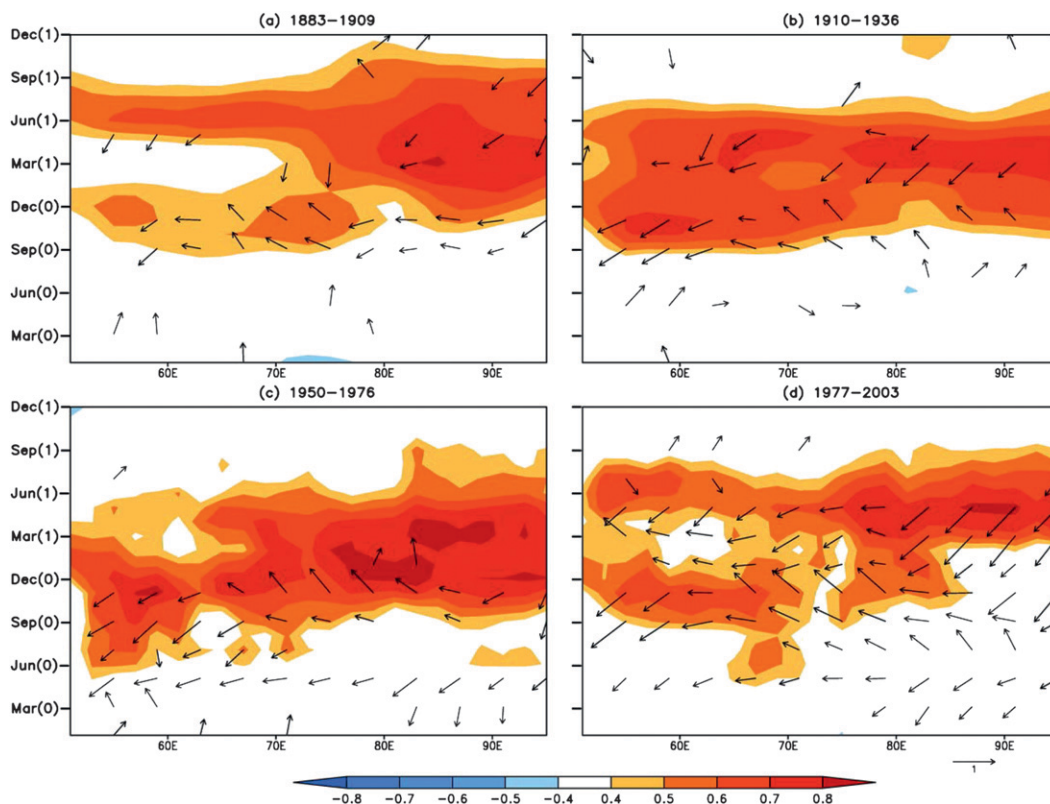
FIG. 6. Correlation of SST (shaded) and surface winds (vectors) along the NIO ship track, with the NDJ(0/1) Niño-3.4 index as a function of calendar month and longitude in (a) epoch 1 (1883–1909), (b) epoch 2 (1910–36), (c) epoch 3 (1950–76), and (d) epoch 4 (1977–2003). Only values exceeding the 90% significance level are displayed (both for shading and vectors).

north of the equator and northwesterlies south of the equator attains its peak phase at the same time (Kawamura et al. 2001; Wu et al. 2008; Wu and Yeh 2010; Du et al. 2009). As the mean wind turns southwesterly in May over the NIO, the northeasterly anomalies oppose the mean southwesterlies and reduce the LHF, giving rise to the second peak of the SST warming in JJA(1). Over the Bay of Bengal, SST warming is delayed by about a season and SW radiation also seems to play a role in maintaining the SST warming in late spring and early summer (Fig. 8d). Overall in most of NIO during JJA(1), northeasterly wind anomalies reduce the southwesterly mean flow to warm the SST because of the reduced AtF-L (Du et al. 2009) in both epochs 1 and 4.

b. Role of southwest tropical Indian Ocean

During El Niño, atmospheric teleconnection forces downwelling Rossby waves in the southern tropical Indian Ocean, which propagate westward (Masumoto and Meyers 1998) and induce SST warming in the southwest tropical Indian Ocean (Xie et al. 2002; Huang and Kinter 2002). At the El Niño mature phase, strong

downwelling Ekman pumping associated with anomalous wind curl in the southeast tropical Indian Ocean forces a downwelling Rossby wave. As the downwelling Rossby waves propagate into the thermocline ridge over the southwest tropical Indian Ocean, they induce positive SST anomalies via thermocline feedback (Xie et al. 2002). The SST warming propagates slowly westward with the oceanic Rossby waves and persists through spring and early summer (Du et al. 2009; Xie et al. 2010). Warm SST anomalies over the southwest tropical Indian Ocean drive an antisymentric wind pattern with northeasterly anomalies over the NIO. These northeasterly anomalies in north of the equator help to warm SST over the NIO as discussed in the previous section by adjusting the heat flux during JJA(1).

Here, we examine the evolution of SST and cloudiness over the southwest tropical Indian Ocean for the twentieth century. Figure 9a shows the correlation of ICOADS SST and cloudiness anomalies averaged between 55°–70°E and 5°–12°S with the NDJ(0/1) Niño-3.4 SST index. Note that, because surface meteorological data are very sparse over the southwest tropical Indian Ocean before
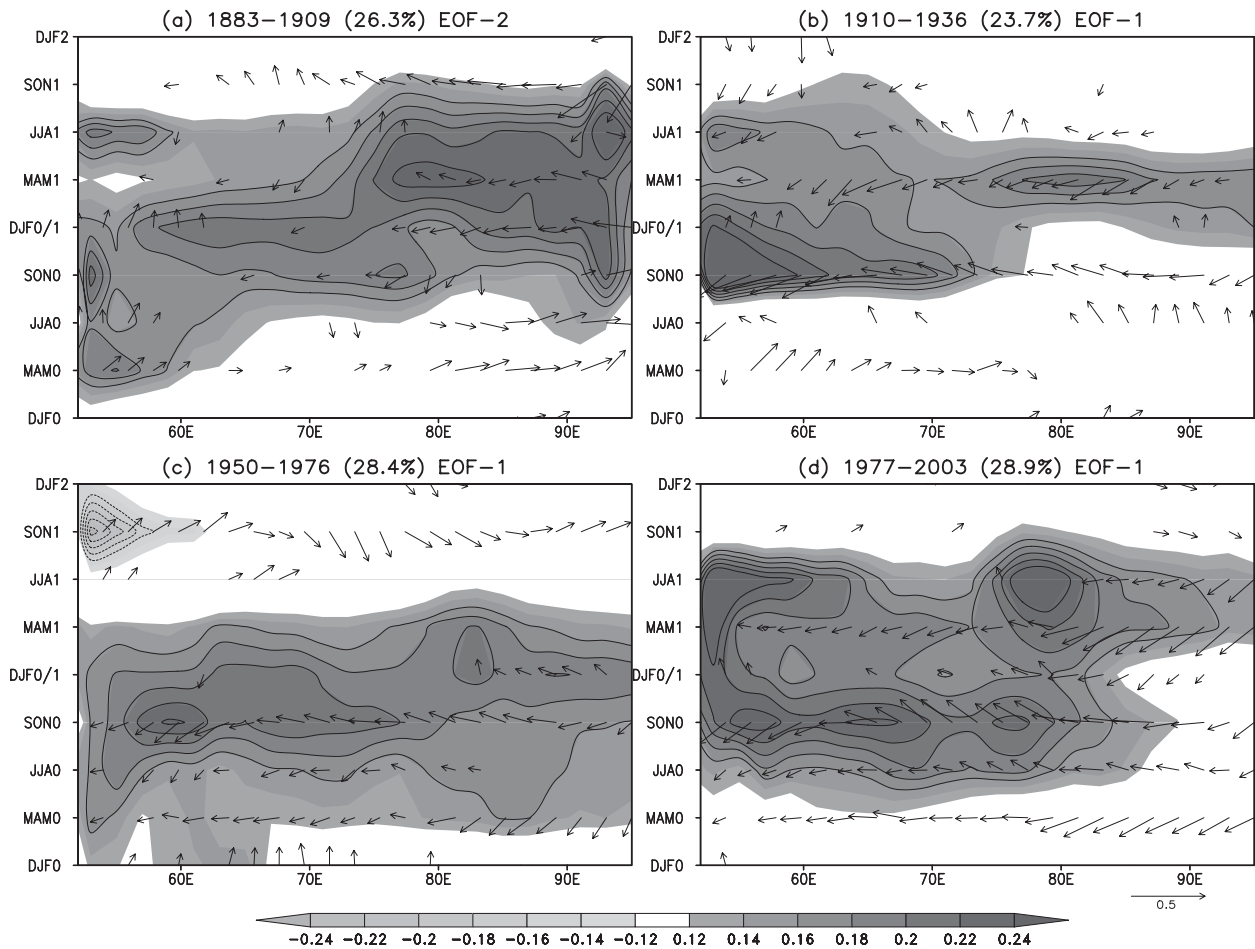
FIG. 7. ENSO-related S-EOFs of NIO ship track SST for the interval from DJF(0) (a year before the mature phase of El Niño) to DJF(2) (a year after the mature phase of El Niño) for (a) epoch 1, (b) epoch 2, (c) epoch 3, and (d) epoch 4. Surface wind anomalies (vectors, m s^{-1}) regressed upon the principal component corresponding to the spatial pattern (shaded) in each epoch. (top) Percentage of variance explained by S-EOF is shown at the top of each panel.

1900 (Fig. 1), our correlation analysis is limited to the period after 1900. The SST warming over the southwest tropical Indian Ocean tends to peak in MAM(1) and, likely in association with downwelling Rossby wave propagation, persists until June(1) in epoch 2 (1910–36). The warming is more pronounced in recent decades and more commonly persists through JJA(1) compared to other epochs. In particular, El Niño decays earlier during epoch 3 compared to epoch 4 (Xie et al. 2010). The slow decay of El Niño helps to sustain the teleconnection forcing longer over the tropical Indian Ocean, causing the strong warming over the southwest tropical Indian Ocean to persist longer. The Indian Ocean dipole mode may have some effect on the southwest tropical Indian Ocean warming on the decadal time scale during the decay phase of ENSO (Rao and Behera 2005; Tozuka et al. 2010). In late spring after April(1) the southwest tropical Indian Ocean warming induces positive precipitation

anomalies by intensifying convection, which is accompanied by cyclonic circulation anomalies (Xie et al. 2002, 2010; Du et al. 2009). This is supported by ICOADS cloudiness (Fig. 9a) and precipitation at Seychelles (4.43°S and 55.31°E) station (Fig. 9b), which shows a peak correlation with ENSO in June(1), significant above 95% level in epochs 2 and 4. This positive correlation between station rainfall and local SST is due to long persistence of the intertropical convergence zone over the warm SST region of the southwest tropical Indian Ocean (Annamalai et al. 2005; Izumo et al. 2008). Enhanced convection over the southwest tropical Indian Ocean contributes to the observed easterly wind anomalies in the NIO during MAM(1) and JJA(1), which are important for the second summer warming over the NIO (Xie et al. 2010). Lack of data makes it difficult to link the southwest tropical Indian Ocean and NIO warming in epoch 1 (before 1900). However, as demonstrated in this
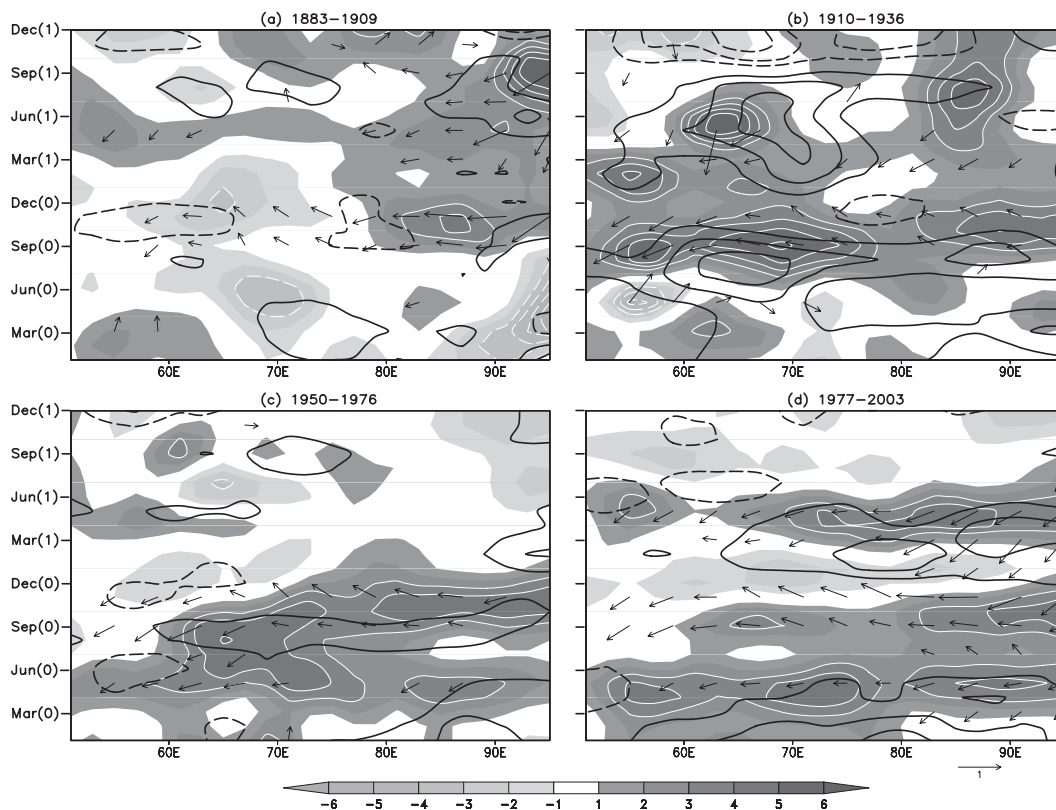
FIG. 8. Regression coefficients of AtF-L (shaded; W m^{-2}), surface winds (vectors; m s^{-1}), and shortwave radiation (contours; W m^{-2}) along the NIO ship track, upon the NDJ(0/1) Niño-3.4 index as a function of calendar month and longitude in (a) epoch 1, (b) epoch 2, (c) epoch 3, and (d) epoch 4. The contour levels for shortwave radiation are ±1, ±2, ±3, and ±4 W m^{-2}, where dashed lines represent negative and solid lines represent positive anomalies.

section, southwest tropical Indian Ocean SST tied with westward-propagating Rossby waves plays a critical role in NIO JJA(1) warming in recent decades, which is consistent with previous studies.

6. South China Sea and northwest Pacific

Interannual SST anomalies in the South China Sea are highly correlated with ENSO (Xie et al. 2003; Liu et al. 2004; Wang et al. 2006; Du et al. 2009). Similar to the NIO warming, South China Sea SST also exhibits apparent interdecadal variability in responses to El Niño during the past century. Figure 10 shows NDJ(0/1) Niño-3.4 index correlations with South China Sea SST and wind anomalies as a function of calendar month. Throughout all epochs, there is a late winter [JF(1)] peak in SST warming. Most importantly, both in epochs 1 and 4 South China Sea SST display a significant warming in the summer following El Niño. In epochs 2 and 3, SST warming is limited to the early summer season in the South China Sea. The double-peak pattern in warming appears in the most recent two epochs, one centered in

late winter and the other in early summer for epoch 3 and in midsummer for epoch 4, as noted by Wang et al. (2006) and Du et al. (2009). Pronounced interdecadal variability in surface winds is evident in the most recent two epochs. Persistent northeasterly winds are prominent in summer during epoch 4 but absent in epoch 3 (Xie et al. 2010). Southerly wind anomalies are dominant during winter in epoch 2 and in epoch 3. The wind pattern is not well organized in epoch 1, possibly due to inadequate surface wind data (see Fig. 1). In winter at the mature phase of El Niño, the South China Sea experiences anomalous descending motion, leading to a decrease in cloudiness and an increase in SW radiation anomalies and thus helping to warm the South China Sea SST (Liu et al. 2004; Wang et al. 2006). In the early summer at the decay phase of El Niño, the anomalous surface northeasterly anomalies oppose the mean southwesterlies and give rise to the pronounced second South China Sea warming peak in epoch 4 (Wang et al. 2006; Du et al. 2009). Ocean dynamics plays a role in South China Sea SST variability, in the central basin off South Vietnam in summer (Xie et al. 2003) and in the southern
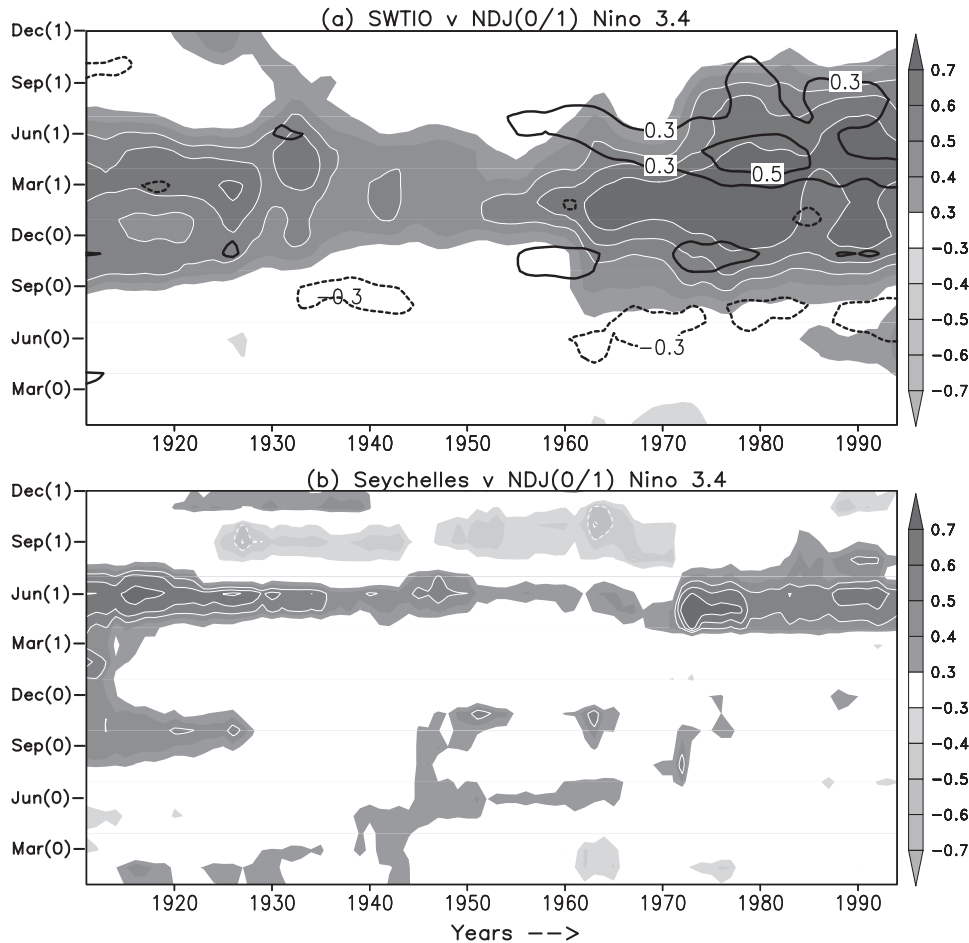
FIG. 9. The 21-yr sliding correlation between NDJ(0/1) Niño-3.4 index and southwest tropical Indian Ocean (a) SST (shaded) and cloudiness (contours) averaged over the area 55°–70°E and 5°–12°S from the ICOADS 2.5 gridded dataset, and (b) Seychelles station rain gauge precipitation (4.43°N and 55.31°E) as a function of calendar month.

basin of Vietnam in winter (Liu et al. 2004). Besides the double-peak pattern, another substantial difference among different epochs is the timing of the onset of significant warming. During epochs 1 and 4, warming starts at the beginning of winter, whereas in epochs 2 and 3 it begins to appear in the fall season. Overall, warming characteristics of the summer after El Niño are similar in epochs 1 and 4 both in the South China Sea and NIO.

At the ENSO decay phase, pronounced atmospheric anomalies are observed over the northwest Pacific (Wang et al. 2000; Xie et al. 2009; Chowdary et al. 2010, 2011). Figure 11 shows correlations of the NDJ(0/1) Niño-3.4 with northwest Pacific SLP and cloudiness along ship track as a function of calendar month. During epoch 1, atmospheric data are very sparse with gaps over the South China Sea and northwest Pacific (Fig. 1). The striking difference among the three most recent epochs over the northwest Pacific is apparent in suppressed rainfall

(negative cloudiness) associated with high SLP in summer after El Niño. Both in epoch 2 and epoch 3, high negative correlations in cloudiness and SLP are noted in late winter and spring at the decay phase of El Niño but do not persist into June(1). During epoch 4 the cloud patterns over this region are very robust at various phases of El Niño. For instance, negative cloudiness anomalies begin to appear around fall, peak in late winter and early spring, and decay after summer. These signals are very prominent between ~10° and 20°N over the northwest Pacific region. Not surprisingly, during the decay phase of El Niño, positive SLP anomalies follow closely the variability of the cloudiness and convection. In this region, convective–circulation feedback is found to be very prominent, especially during summer following El Niño (Xie et al. 2009, 2010; Chowdary et al. 2010).

The Philippines and Guam are located in the subtropical northwest Pacific region that tends to experience rainfall
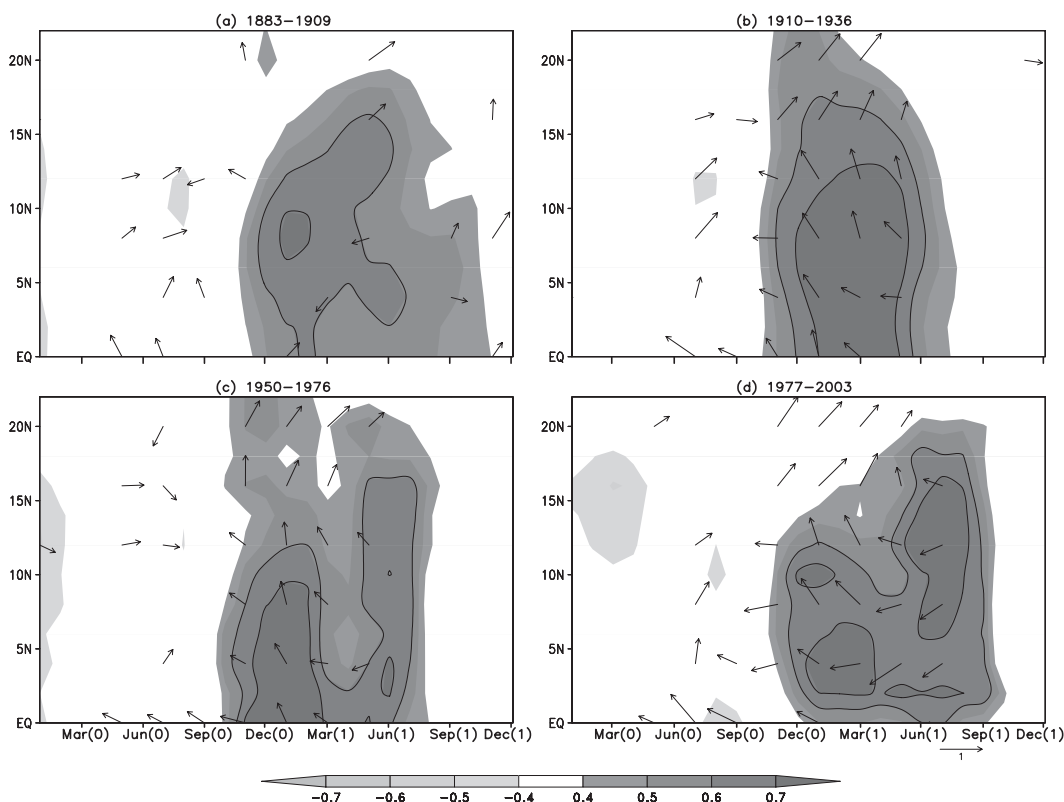
FIG. 10. Correlation of SST (shaded) and surface winds (vectors) along the South China Sea ship track, with the NDJ(0/1) Niño-3.4 index as a function of calendar month and latitude for (a) epoch 1, (b) epoch 2, (c) epoch 3, and (d) epoch 4. Only values exceeding the 90% significance level are displayed (both for shading and vectors).

deficits during the decay phase of El Niño from winter to early summer. Here we analyze historical rain gauge data for the Philippines and Guam from 1900 to 2007 to corroborate interdecadal modulation of the ENSO teleconnection. As seen in the northwest Pacific ship track cloudiness analysis, negative rainfall anomalies begin around fall [SON(0)] in response to El Niño over the Philippines (Fig. 12). This negative rainfall response ends around early summer at the beginning and end of the (epoch 4) twentieth century. This Philippine rainfall variability in the summer following El Niño in recent decades is consistent with the findings of Xie et al. (2010). Guam is located at 13.6°N and 144.8°E, which is almost at the center of negative precipitation anomalies during summer after El Niño. As shown in Fig. 12, significant negative precipitation anomalies at Guam extend to JJA(1) at the end of the twentieth century. Similar negative rainfall anomalies are seen at the beginning of the twentieth century but are significant at 90% confidence level only until early summer. Epoch 3, starting from 1950s, features low correlations in summer following El Niño.

Furthermore, to examine the spatial pattern of summer rainfall we use land rainfall data from Dai et al. (1997) for

the first three epochs and CMAP data (both land and ocean) for the most recent epoch. Figure 13 shows the spatial pattern of JJA(1) precipitation correlation with the NDJ(0/1) Niño-3.4 index. During epochs 1 and 4, there are significant negative correlations over the Philippines, consistent with the station rainfall analysis for epoch 4. The negative correlations are weak or replaced by weak positive correlations for epochs 2 and 3 over this region. We notice considerable positive rainfall correlations on the west coast of the Indian subcontinent, a finding complementary to previous studies that focus on the summer of El Niño developing years during both epochs 1 and 4. The rainfall correlations over Japan are positive during JJA(1) in epochs 1 and 4 but turn negative in epochs 2 and 3. Rainfall correlations over China, marginally significant for each epoch, are also variable in pattern. Land rainfall analysis further supports the idea that there are considerable interdecadal changes in the Indo–western Pacific response to ENSO. Our analyses of various datasets confirm the fact that the teleconnection between ENSO (at its decay phase) and the Indo–western Pacific is strong in summer during JJA(1) for both epochs 1 and 4 compared with the other two epochs.
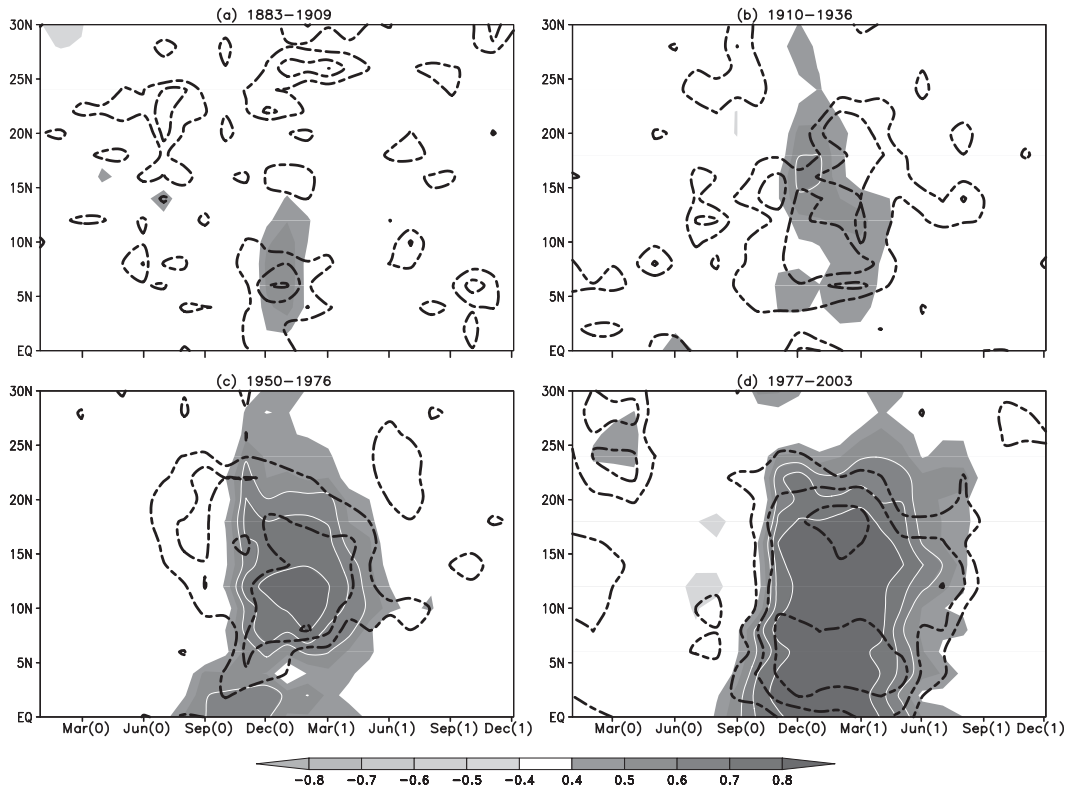
FIG. 11. Correlation of SLP (shaded) and cloudiness (contours) along the northwest Pacific ship track (east of the Philippines) with the NDJ(0/1) Niño-3.4 index as a function of calendar month and latitude for (a) epoch 1, (b) epoch 2, (c) epoch 3, and (d) epoch 4. Contours for cloudiness correlations are shown at values of ±0.4, ±0.5, ±0.6, and ±0.7, with solid (dashed) contours indicating positive (negative) correlations. White counters indicate a correlation magnitude above 0.7. Only values exceeding the 90% significance level are displayed.

7. Analysis of TOGA CAM3 simulations

Because of its relatively slow variations, SST is generally better observed than sparse meteorological measurements prior to 1950. Forced by observed SST, atmospheric GCMs show skills in simulating ENSO teleconnections and their interdecadal modulation (e.g., Huang et al. 2010). To complement our observational analysis, we
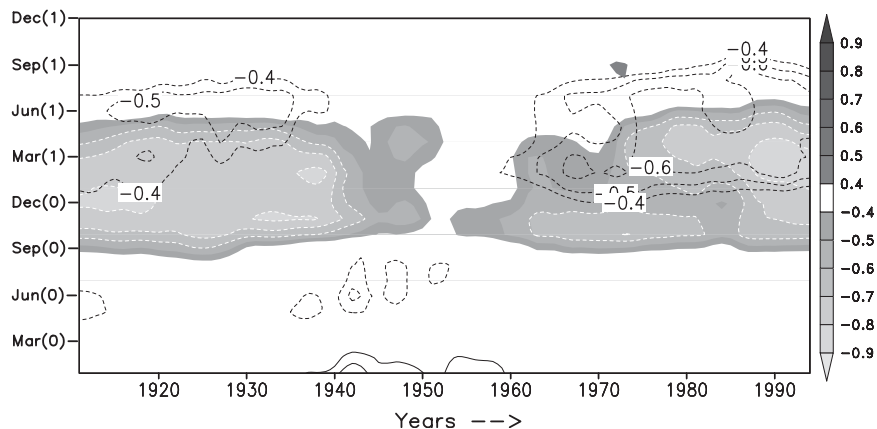

FIG. 12. The 21-yr sliding correlations between the NDJ(0/1) Niño-3.4 index and averaged station precipitation of Philippines (shaded) and Guam (13.24°N and 144.38°E; contours) with as a function of calendar month. Only values exceeding the 90% significance level are displayed.
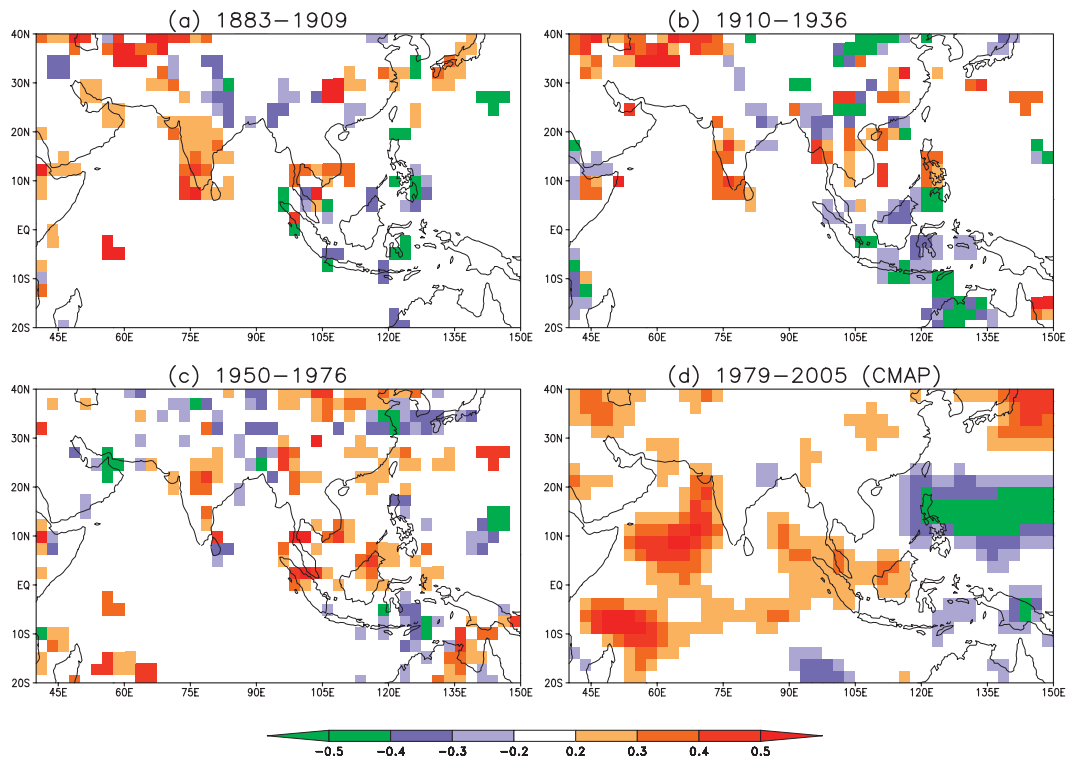
FIG. 13. The JJA(1) correlation of land precipitation with the NDJ(0/1) Niño-3.4 index in (a) epoch 1, (b) epoch 2, (c) epoch 3, and (d) epoch 4. Land precipitation data are from Dai et al. (1997) for first three epochs, and in epoch 4 precipitation data are obtained from CMAP.

examine the ensemble mean of five simulations from an AGCM forced with TOGA SST from 1871 to 2000. Figure 14 shows the ENSO correlation with JJA(1) SST, SLP, and surface wind velocity from the ensemble mean of the CAM3 TOGA run. Note that during the most recent epoch, model data are available for a shorter period of only 24 years instead of 27 years. Five AGCM integrations (ensemble members) may be adequate for the tropical response, especially for correlation analysis. Correlation maps between NDJ(0/1) Niño-3.4 and JJA(1) SLP for ensemble members and ensemble mean shows (Figure not shown) that individual ensemble patterns of SLP over the Indo–western Pacific during JJA(1) are somewhat similar to the ensemble mean patterns. Time series of JJA SLP anomaly over the northwest Pacific region for ensemble mean and individual members also indicate that spread among ensemble members is small (not shown). Standard deviation of SLP time series is between 0.41 and 0.48 among ensemble members including ensemble mean and correlation between ensemble members and mean is >0.75.

The SST displays warming north of the Maritime Continent and over the tropical Indian Ocean mainly in epochs 1 and 4 and to some extent in epoch 2 (Fig. 14). The model reproduces the main features of

the Indo–western Pacific teleconnections during the summer following El Niño well in comparison with observations (e.g., Xie et al. 2009). Chowdary et al. (2011) conducted a pair of experiments using a coupled GCM, one with an interactive air–sea coupling in the tropical Indian Ocean and one prescribing climatological SST. The AGCM circulation patterns in the present paper are consistent with coupled model experiment result. Specifically, the model shows a strong anticyclonic circulation in the northwest Pacific region both in epochs 1 and 4. Basinwide warming over the tropical Indian Ocean appears strong during epoch 2 but the northwest anticyclonic circulation seems weak. This may be due to the presence of significant warm SST anomalies east of the Philippines, which act to push the center of the northwest Pacific high pressure eastward in epoch 2 as compared to epochs 1 and 4. In addition, the equatorial Pacific warming weakens the off-equatorial high pressure anomalies via Rossby wave mechanism. During epoch 3, basinwide tropical Indian Ocean warming is very weak in JJA(1), and as noted by earlier studies (Huang et al. 2010; Xie et al. 2010), both the anticyclone and SLP high over the northwest Pacific shifted slightly to the east of 120°E and weakened in magnitude. SST warming over the NIO in different epochs is consistent with ship track data during JJA(1) (Fig. 6).
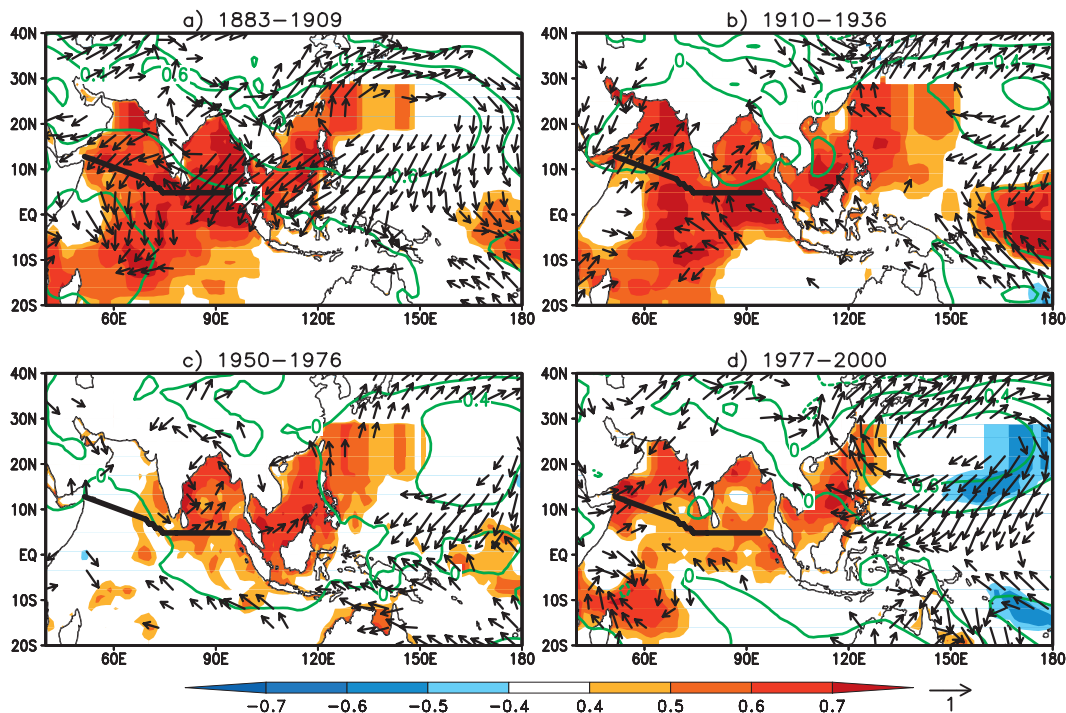
FIG. 14. The NDJ(0/1) Niño-3.4 SST index correlation with JJA(1) SST (shaded), SLP (contours), and surface wind velocity (vectors) from the ensemble mean of the CAM3 run for (a) epoch 1, (b) epoch 2, (c) epoch 3, and (d) epoch 4. NIO ship track is superimposed on model SST anomalies (thick black line). Only values exceeding the 90% significance level are displayed (both for shading and vectors).

Forced with observed SST, AGCMs have difficulty simulating Asian–Pacific summer monsoon rainfall properly (Wang et al. 2005). By contrast, JJA(1) rainfall patterns are fairly well simulated over the Indo–western Pacific region in the current AGCM. When correlated with NDJ(0/1) Niño-3.4 index, model JJA(1) precipitation correlations display similar features compared to observations in recent decades (Figs. 13d and 15d). Negative rainfall correlations over the northwest Pacific and positive anomalies over the tropical Indian Ocean and the Maritime Continent are fairly well reproduced. Model JJA(1) tropospheric temperature is similar to that described by Xie et al. (2009) in observations, with a Kelvin wave–like wedge propagating from the tropical Indian Ocean to the equatorial western Pacific. No reliable observations of tropospheric temperature exist prior to 1950 and therefore model tropospheric temperature simulations are very important. The capacitor effect (Xie et al. 2009) described below is well represented by the AGCM results. The tropical Indian Ocean surface warming causes tropospheric temperature to increase via deep convection, emanating a baroclinic Kelvin wave into the equatorial Pacific. The warm Kelvin wave wedge lowers the SLP in the equatorial western Pacific, inducing northeasterly surface wind anomalies over the

subtropical northwest Pacific (Fig. 14). The resultant divergence in the subtropics suppresses convection, and the convective and circulation anomalies amplify via their interaction. Thus, a strong tropical Indian Ocean response translates into a pronounced development of atmospheric anomalies over the northwest Pacific and East Asia during JJA(1) as the direct influence of ENSO fades. Similar features are noted in epochs 1 and 4 in the model simulations and are supported by the analysis based on ship observations. In epoch 2, the rainfall and tropospheric temperature distribution in JJA(1) in response to El Niño are not as well organized as in either epoch 1 or 4. In the case of epoch 3, the Kelvin wave wedge in tropospheric temperature is somewhat clear but the meridional gradient $[\partial(\mathrm{TT})/\partial y]$ is small near the Philippines. This seemingly explains why rainfall anomalies are weak over the northwest Pacific.

The results presented so far suggest that the most robust atmospheric signals are evident over the northwest Pacific in the summer following El Niño both in observations and in the model. Earlier studies reported that the northwest Pacific JJA(1) atmospheric anomalies (such as precipitation, SLP, and winds) are highly predictable in coupled models and also emerge as one of the leading modes in interannual variability (Wang et al.
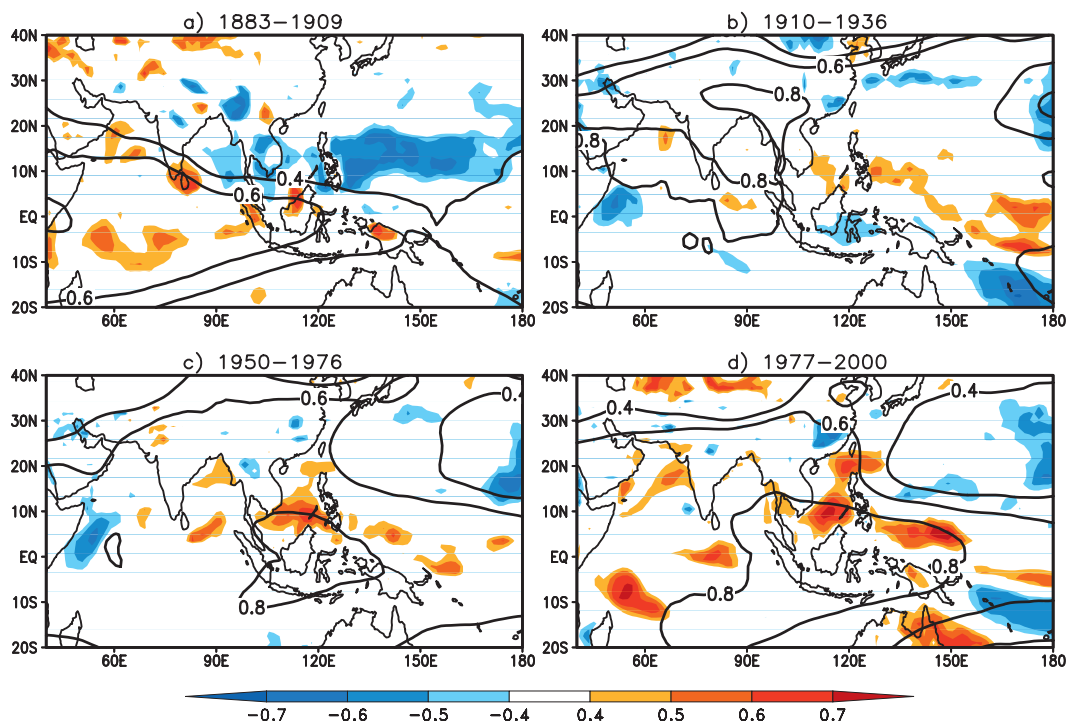
FIG. 15. As in Fig. 14, but for precipitation (shaded) and tropospheric temperature (contours). Note that tropospheric temperature is represented by the geopotential height difference between 200 and 500 hPa.

2009; Chowdary et al. 2010, 2011). The leading EOF patterns corresponding to JJA(1) SLP and rainfall over the northwest Pacific are well represented in the model for all four epochs (not shown).

8. Discussion: Causes of interdecadal change in ENSO teleconnection

Our results suggest that there is clear interdecadal modulation of interannual variability in the Indo–western Pacific region in relation to ENSO over the past 130 years. What causes such interdecadal–epochal change in ENSO-induced anomalies? Are the epochal changes described in the present study part of ongoing global warming? Xie et al. (2010) hint at the possible mechanism that gives some sign of the global warming effect on the recent strengthening of ENSO teleconnections to the Indo–western Pacific at the ENSO decay phase based on data analysis of the past 60 years. The secular warming of the tropical Indian Ocean since the 1950s (Du and Xie 2008) may enhance the convective and tropospheric temperature response to interannual anomalies of the tropical Indian Ocean SST. The enhanced ocean temperature stratification helps strengthen the tropical Indian Ocean basin mode warming response to El Niño by shoaling the mixed layer and intensifying thermocline feedback in

upwelling regions such as the southwest tropical Indian Ocean (Xie et al. 2010). This secular warming may have some influence on the ENSO teleconnections to the Indian Ocean in the recent epoch. Indeed, Zheng et al. (2011) show that El Niño–induced tropical Indian Ocean warming and the anomalous anticyclone in the northwest Pacific persist for a long period of time in a coupled GCM that simulates global warming in response to induced GHG.

Looking back into historical data more than a century provides a perspective about whether these teleconnection changes are related to climate change or to natural variability. A strong ENSO teleconnection to the Indo–western Pacific region occurs during JJA(1) in epochs 1 and 4. For example, Fig. 16a illustrates the 21-yr sliding correlation of JJA NIO SST (ship) and northwest Pacific SLP (CAM3 run) anomalies with the NDJ(0/1) Niño-3.4 index for the entire period. Strong correlation between summer NIO SST and the Niño-3.4 index are observed in epochs 1 and 4. A similar ENSO teleconnection with the northwest Pacific SLP is also evident during the same periods. Note that the NIO SST correlation is very much in phase with northwest Pacific SLP, showing the Indian Ocean impact on northwest Pacific climate in JJA(1) as in Huang et al. (2010) and Xie et al. (2010). However, it appears that epochal changes in teleconnections may not necessarily be attributed to climate change as strong ENSO–western
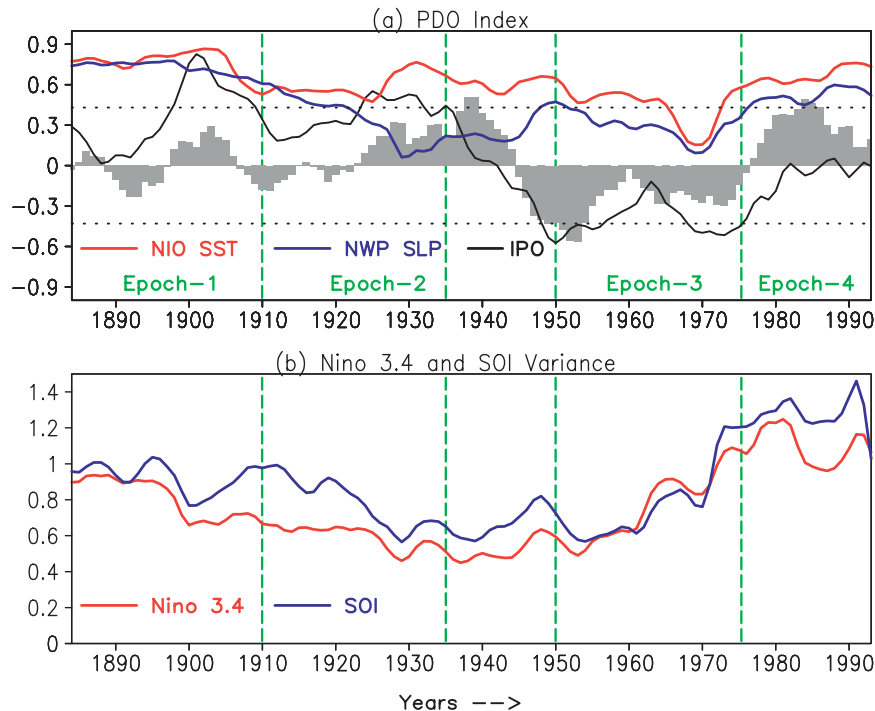
FIG. 16. (a) The time series of the PDO index (scaled by 2; gray bars), the IPO index (black line), and 21-yr sliding correlations of NDJ(0/1) Niño-3.4 index with the JJA(1) NIO SST (averaged along ship track; red line) and northwest Pacific SLP principal component (CAM3 run; blue line). (b) Time series of NDJ(0/1) Niño-3.4 index (red line) and DJF(0/1) SOI (scaled by 2.8; blue line) variance in 21-yr sliding windows. Dotted lines denote the 95% significance level for sliding correlations in (a). Green dashed lines indicate different epochs as in Fig. 5.

Pacific teleconnections in JJA(1) exist not only in epoch 1 but also in epoch 4.

Another hypothesis for variations in ENSO impacts involves variations in the PDO (Mantua et al. 1997; Gershunov and Barnett 1998). The PDO is defined here as the leading EOF of North Pacific SST (north of 20°N) for the extended winter (November–March) from 1900 to 2009. Both the seasonal cycle and global mean SST are removed at each grid point prior to the EOF analysis. The PDO index is generated by projecting North Pacific SST for all months from 1870 to 2009 and then standardizing the resulting time series. The time series of the PDO (5-yr smoothing is applied) is in-phase with the modulation of ENSO teleconnections to the summer Indo–western Pacific in the two most recent epochs starting from 1950s (Fig. 16a). ENSO teleconnections are weak during the negative phase of PDO in epoch 3 (1950–mid-1970s) but strong during the positive phase of the PDO (epoch 4). This is consistent with some earlier studies suggesting PDO modulation of ENSO correlations with Australia precipitation (Power et al. 1999) and with the East Asia winter monsoon (L. Wang et al. 2008). However, the relationship between the PDO and

the correlation between the Niño-3.4 index and the Indo–western Pacific is very weak prior to the 1950s.

The IPO (Power et al. 1999) index is plotted along with the PDO index in Fig. 16a. The IPO index is calculated based on a procedure as in Parker et al. (2007). Similar to the PDO index, IPO also displayed some coherence with ENSO teleconnections to the Indo–western Pacific after 1950s. In the late nineteenth and the first-half of the twentieth century, the IPO is not correlated with ENSO teleconnections. This shows that epochal changes of ENSO teleconnections to the Indo–western Pacific in summer is more complicated than previously thought. Apart from PDO and IPO, decadal ENSO-like mode also exhibits some impact on the climate of the Indian Ocean and adjacent landmasses on a range of decadal to multidecadal time scale (Allan and D'Arrigo 1999; Allan et al. 2003).

To examine if ENSO variability itself is responsible for changes in decadal teleconnection patterns, we present NDJ(0/1) Niño-3.4 and SOI variance in 21-yr windows (Fig. 16b). ENSO variance as measured both by SST and SOI is in phase with JJA(1) tropical Indian Ocean/NIO SST warming (Fig. 5) along with northwest
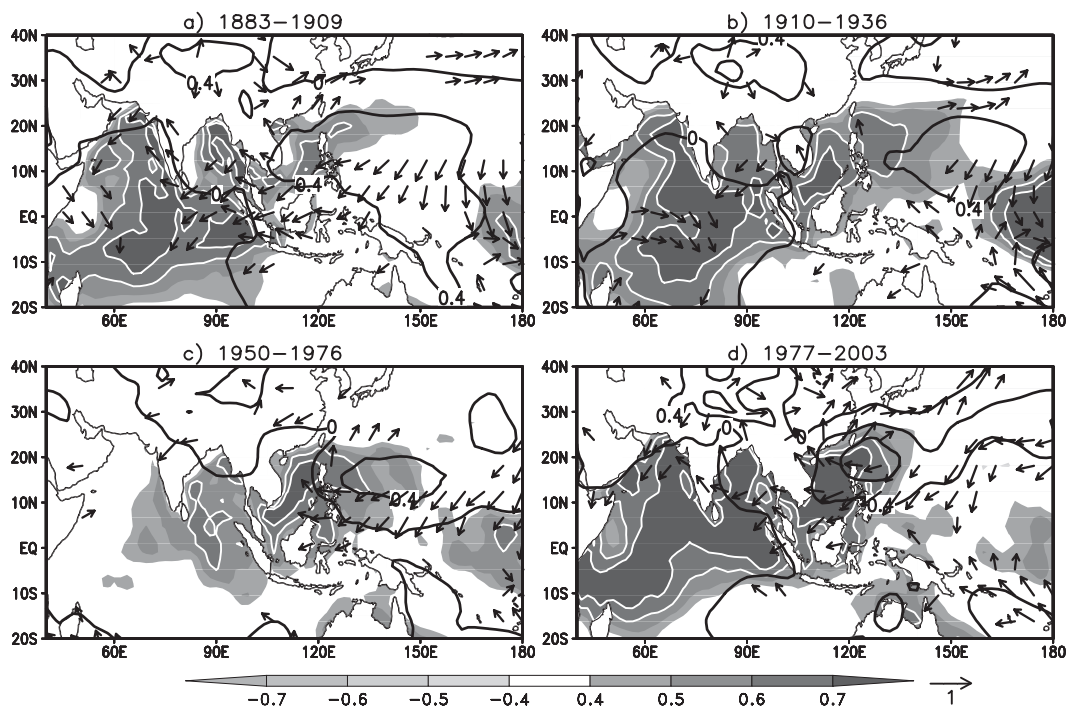
FIG. A1. The NDJ(0/1) Niño-3.4 SST index correlation with JJA(1) 2-m temperature (shaded), SLP (contours), and surface wind velocity (vectors) from 20CR in (a) epoch 1, (b) epoch 2, (c) epoch 3, and (d) epoch 4. Only values exceeding the 90% significance level are displayed.

Pacific atmospheric anomalies. Specifically, NDJ(0/1) Niño-3.4 El Niño variance is high after the 1970s and before the 1920s, two epochs when ENSO teleconnections to the Indo–western Pacific are strong, especially in summer following El Niño. The period, amplitude, spatial structure, and temporal evolution of El Niño events can significantly change teleconnections (Diaz et al. 2001). This study shows that the centennial change in El Niño variance is important for epochal changes in ENSO's influence on the Indo–western Pacific. The strengthening of the summer ENSO influence on the Indo–western Pacific in recent decades and late in the 1800s may be a part of natural variability of the ocean–atmosphere system.

9. Summary

We have studied the centennial modulation of interannual variability over the Indo–western Pacific and its relationship to ENSO for 1870–2007 through the innovative use of surface meteorological observations along a busy ship track across the north Indian Ocean and South China Sea. Four epochs, 1883–1909 (epoch 1), 1910–36 (epoch 2), 1950–76 (epoch 3), and 1977–2003 (epoch 4) are chosen based on the seasonal evolution of NIO SST warming associated with ENSO. The period

during and shortly after World War II is not examined in detail because of insufficient data.

El Niño–induced warming in the NIO is found to display a double-peak pattern in time during epochs 1 and 4 and is especially prominent in the Arabian Sea (west of 75°E). These results are supported by S-EOF analysis for different epochs. The second peak of the NIO warming in summer following El Niño is primarily driven by air–sea interactions within the tropical Indian Ocean. Warming in the southwest tropical Indian Ocean drives the northeasterly anomalies over the NIO. In the latter region easterly wind anomalies intensify the northeast monsoon mean winds and cool the SST because of latent heat fluxes in winter and early spring after El Niño in epoch 4. As the mean wind turns southwesterly in April and May over the NIO, northeasterly anomalies oppose the mean southwesterlies, and the reduced latent heat flux gives rise to the SST warming in JJA(1). This mechanism is similar to that of Du et al. (2009). The warming in the NIO during JJA(1) is of interest because it anchors the northwest Pacific anticyclonic circulation (Xie et al. 2009) and reduces the number of tropical cyclones in the latter region (Du et al. 2011).

Our analysis reveals that ENSO teleconnections to the Indo–western Pacific in the spring and summer following El Niño has strengthened in the most recent
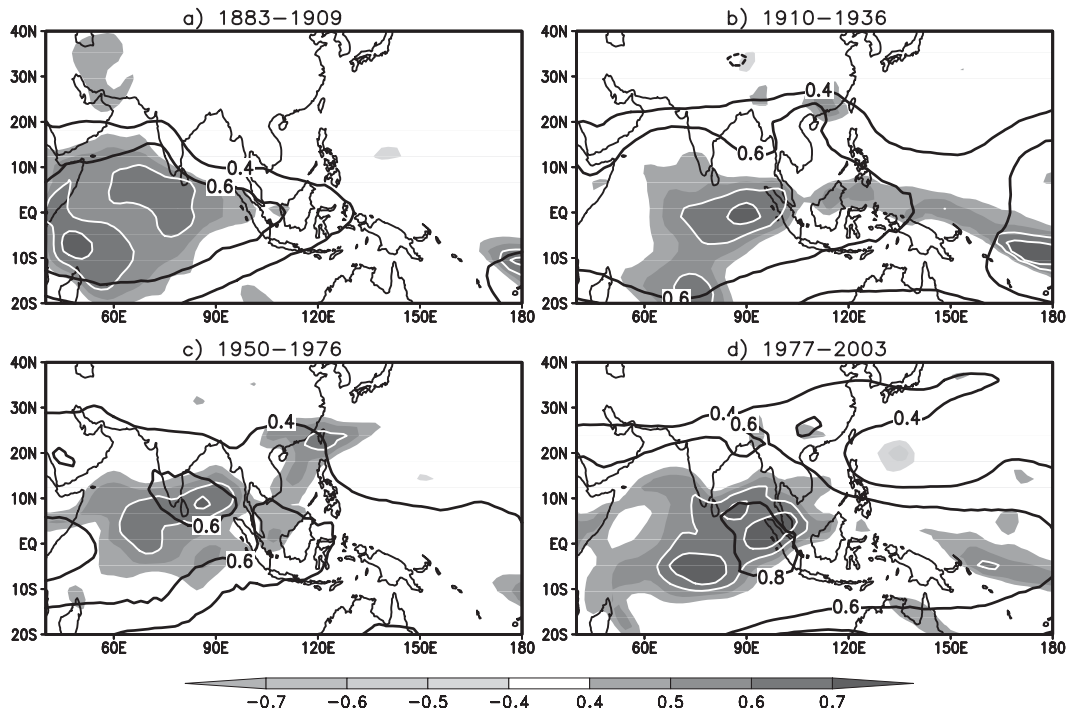
FIG. A2. As in Fig. A1, but for precipitable water (shaded) and tropospheric temperature (contours). Tropospheric temperature is represented by the geopotential height difference between 200 and 850 hPa.

decades, which is consistent with previous studies (Xie et al. 2010). Similarly strong teleconnections are also observed in epoch 1 between the late nineteenth and early twentieth centuries. SST warming over the Indo–western Pacific, the development of northwest Pacific anticyclonic circulation anomalies, and the tropospheric temperature distribution are the most robust anomalies associated with ENSO during the summer following El Niño. During epochs 2 and 3 the ENSO teleconnection to the northwest Pacific is weak during JJA(1), a result corroborated by island observations at Guam and the Philippines. The AGCM forced with observed SST (TOGA) anomalies reproduces such epochal changes. Specifically, the northwest Pacific anticyclone is weak and shifted to east of 120°E during epochs 2 and 3. These results are also reflected in the twentieth-century reanalysis (see appendix).

The strengthening and weakening of the ENSO influence on the Indo–western Pacific region during spring and summer following El Niño in different epochs are related to variations with El Niño. The decadal changes in ENSO teleconnection coincide with that of the PDO and IPO after the 1950s, but this correlation breaks down prior to 1950s. Our results suggest that this decadal modulation of teleconnections associated with ENSO over the Indo–western Pacific is governed primarily by ENSO variance. A recent study based on North American tree rings

showed that interdecadal modulation of ENSO amplitude has been common for the past millennium (Li et al. 2011). The strengthening of ENSO influence on the Indo–western Pacific in recent decades and in the late 1800s may be a part of natural variability of the ocean–atmosphere system. This shows that the most recent epochal change of strengthening in ENSO–Indo–western Pacific correlation are most likely not outside the range of natural variability. It is still interesting to ask how global warming affects ENSO teleconnection to the Indo–western Pacific (Zheng et al. 2011). Future studies need to investigate physical mechanisms for slow modulation of ENSO and its teleconnections.

APPENDIX

Twentieth-Century Reanalysis

Decadal changes in ENSO teleconnection to the Indo–western Pacific are evident in both ship observations and atmospheric model simulations. Here, we analyze the 20CR data from 1871 to 2008 to verify whether such decadal change exists in reanalysis data and is similar to our observations. Figure A1 shows correlations of JJA(1) 2-m temperature, SLP, and 850-hPa wind anomalies with the NDJ(0/1) Niño-3.4 SST index in different epochs. Over the tropical Indian Ocean, SST displays basin-wide warming during JJA(1) in epochs 1, 2, and 4. The northwest Pacific SLP high and the surface anticyclonic circulation are well organized in epochs 1 and 4 but the correlation is low compared to both the model and observation. In response to tropical Indian Ocean SST warming, tropospheric temperature displays a Matsuno (1966)–Gill (1980) pattern, with a Rossby wave response to the west and a warm Kelvin wave propagating to the equatorial western Pacific in both epochs 1 and 4 (Fig. A2). Positive precipitable water anomalies are relatively strong in epochs 1 and 4 compared to the other two epochs over the tropical Indian Ocean. The robust patterns of JJA(1) atmospheric anomalies in the Indo–western Pacific associated with ENSO in different epochs are fairly well represented in the 20CR analysis as compared to our observational study.

REFERENCES

Alexander, M. A., I. Bladé, M. Newman, J. R. Lanzante, N. C. Lau, and J. D. Scott, 2002: The atmospheric bridge: The influence of ENSO teleconnections on air–sea interaction over the global oceans. *J. Climate,* **15,** 2205–2231.

Allan, R. J., and R. D. D'Arrigo, 1999: 'Persistent' ENSO sequences: How unusual was the 1990–1995 El Niño. *Holocene,* **9,** 101–118.

——, N. Nicholls, P. D. Jones, and I. J. Butterworth, 1991: A further extension of the Tahiti–Darwin SOI, early SOI results, and Darwin pressure. *J. Climate,* **4,** 743–749.

——, J. A. Lindesay, and C. J. C. Reason, 1995: Multidecadal variability in the climate system over the Indian Ocean region during the austral summer. *J. Climate,* **8,** 1853–1873.

——, C. J. C. Reason, J. A. Lindesay, and T. J. Ansell, 2003: 'Protracted' ENSO episodes and their impacts in the Indian Ocean region. *Deep-Sea Res. II,* **50,** 2331–2347.

Annamalai, H., P. Liu, and S.-P. Xie, 2005: Southwest Indian Ocean SST variability: Its local effect and remote influence on Asian monsoons. *J. Climate,* **18,** 4150–4167.

——, H. Okajima, and M. Watanabe, 2007: Possible impact of the Indian Ocean SST on the Northern Hemisphere circulation during El Niño. *J. Climate,* **20,** 3164–3189.

Ashok, K., S. K. Behera, S. A. Rao, H. Weng, and T. Yamagata, 2007: El Niño Modoki and its possible teleconnection. *J. Geophys. Res.,* **112,** C11007, doi:10.1029/2006JC003798.

Behera, S. K., P. S. Salvekar, and T. Yamagata, 2000: Simulation of interannual SST variability in the tropical Indian Ocean. *J. Climate,* **13,** 3487–3499.

Chowdary, J. S., and C. Gnanaseelan, 2007: Basinwide warming of the Indian Ocean during El Niño and Indian Ocean dipole years. *Int. J. Climatol.,* **27,** 1421–1438.

——, S.-P. Xie, J. Y. Lee, Y. Kosaka, and B. Wang, 2010: Predictability of summer Northwest Pacific climate in eleven coupled model hindcasts: Local and remote forcing. *J. Geophys. Res.,* **115,** D22121, doi:10.1029/2010JD014595.

——, ——, J.-J. Luo, J. Hafner, S. Behera, Y. Masumoto, and T. Yamagata, 2011: Predictability of Northwest Pacific climate during summer and the role of the tropical Indian Ocean. *Climate Dyn.,* **36,** 607–621, doi:10.1007/s00382-009-0686-5.

Collins, W. D., and Coauthors, 2006: The formulation and atmospheric simulation of the Community Atmosphere Model version 3 (CAM3). *J. Climate,* **19,** 2144–2161.

Compo, G. P., and Coauthors, 2011: The Twentieth Century Reanalysis project. *Quart. J. Roy. Meteor. Soc.,* **137,** 1–28.

Dai, A., I. Y. Fung, and A. D. Del Genio, 1997: Surface observed global land precipitation variations during 1900–88. *J. Climate,* **10,** 2943–2962.

de Szoeke, S. P., S.-P. Xie, T. Miyama, K. J. Richards, and R. J. O. Small, 2007: What maintains the SST front north of the eastern Pacific equatorial cold tongue? *J. Climate,* **20,** 2500–2514.

Diaz, H. F., M. P. Hoerling, and J. K. Eischeid, 2001: ENSO variability, teleconnections, and climate change. *Int. J. Climatol.,* **21,** 1845–1862.

Du, Y., and S.-P. Xie, 2008: Role of atmospheric adjustments in the tropical Indian Ocean warming during the 20th century in climate models. *Geophys. Res. Lett.,* **35,** L08712, doi:10.1029/2008GL033631.

——, ——, G. Huang, and K.-M. Hu, 2009: Role of air–sea interaction in the long persistence of El Niño–induced north Indian Ocean warming. *J. Climate,* **22,** 2023–2038.

——, L. Yang, and S.-P. Xie, 2011: Tropical Indian Ocean influence on northwest Pacific tropical cyclones in summer following strong El Niño. *J. Climate,* **24,** 315–322.

Folland, C. K., and D. E. Parker, 1995: Correction of instrumental biases in historical sea surface temperature data. *Quart. J. Roy. Meteor. Soc.,* **121,** 319–367.

Gershunov, A., and T. P. Barnett, 1998: Interdecadal modulation of ENSO teleconnections. *Bull. Amer. Meteor. Soc.,* **79,** 2715–2725.

Gill, A. E., 1980: Some simple solutions for heat-induced tropical circulation. *Quart. J. Roy. Meteor. Soc.,* **106,** 447–462.

——, 1982: *Atmosphere–Ocean Dynamics.* Academic Press, 120 pp.

Huang, B., and J. L. Kinter III, 2002: Interannual variability in the tropical Indian Ocean. *J. Geophys. Res.,* **107,** 3199, doi:10.1029/2001JC001278.

Huang, G., K. Hu, and S.-P. Xie, 2010: Strengthening of tropical Indian Ocean teleconnection to the northwest Pacific since the mid-1970s: An atmospheric GCM study. *J. Climate,* **23,** 5294–5304.

Hurrell, J. W., J. J. Hack, D. Shea, J. M. Caron, and J. Rosinski, 2008: A new sea surface temperature and sea ice boundary data set for the Community Atmosphere Model. *J. Climate,* **21,** 5145–5153.

Ishii, M., A. Shouji, S. Sugimoto, and T. Matsumoto, 2005: Objective analyses of sea surface temperature and marine meteorological variables for the 20th century using ICOADS and the Kobe collection. *Int. J. Climatol.,* **25,** 865–879.

Izumo, T., C. B. Montégut, J. J. Luo, S. K. Behera, S. Masson, and T. Yamagata, 2008: The role of the western Arabian Sea

upwelling in Indian monsoon rainfall variability. *J. Climate,* **21,** 5603–5623.

Kaplan, A., M. A. Cane, Y. Kushnir, A. C. Clement, M. B. Blumenthal, and B. Rajagopalan, 1998: Analyses of global sea surface temperature 1856–1991. *J. Geophys. Res.,* **103,** 18 567–18 589.

Kawamura, R., T. Matsuura, and S. Iizuka, 2001: Role of equatorially asymmetric sea surface temperature anomalies in the Indian Ocean in the Asian summer monsoon and El Niño–Southern Oscillation coupling. *J. Geophys. Res.,* **106,** 4681–4693.

Kim, K.-Y., and Q. Wu, 1999: A comparison study of EOF techniques: Analysis of nonstationary data with periodic statistics. *J. Climate,* **12,** 185–199.

Kinter, J. L., K. Miyakoda, and S. Yang, 2002: Recent change in the connection from the Asian monsoon to ENSO. *J. Climate,* **15,** 1203–1215.

Klein, S. A., B. J. Soden, and N.-C. Lau, 1999: Remote sea surface temperature variations during ENSO: Evidence for a tropical atmospheric bridge. *J. Climate,* **12,** 917–932.

Kubota, H., and J. C. L. Chan, 2009: Interdecadal variability of tropical cyclone landfall in the Philippines from 1902 to 2005. *Geophys. Res. Lett.,* **36,** L12802, doi:10.1029/2009GL038108.

Kumar, K. K., B. Rajagopalan, and M. A. Cane, 1999: On the weakening relationship between the Indian monsoon and ENSO. *Science,* **284,** 2156–2159.

Lau, N.-C., and M. J. Nath, 2000: Impact of ENSO on the variability of the Asian–Australian monsoons as simulated in GCM experiments. *J. Climate,* **13,** 4287–4309.

Li, J., S.-P. Xie, E. R. Cook, G. Huang, R. D'Arrigo, F. Liu, J. Ma, and X. Zheng, 2011: Interdecadal modulation of El Niño amplitude during the past millennium. *Nat. Climate Change,* **1,** 114–118, doi:10.1038/nclimate1086.

Liu, Q., X. Jiang, S.-P. Xie, and W. T. Liu, 2004: A gap in the Indo-Pacific warm pool over the South China Sea in boreal winter: Seasonal development and interannual variability. *J. Geophys. Res.,* **109,** C07012, doi:10.1029/2003JC002179.

Mantua, N. J., S. R. Hare, Y. Zhang, J. M. Wallace, and R. C. Francis, 1997: A Pacific interdecadal climate oscillation with impacts on salmon production. *Bull. Amer. Meteor. Soc.,* **78,** 1069–1079.

Masumoto, Y., and G. Meyers, 1998: Forced Rossby waves in the southern tropical Indian Ocean. *J. Geophys. Res.,* **103,** 27 589–27 602.

Matsuno, T., 1966: Quasi-geostrophic motions in the equatorial area. *J. Meteor. Soc. Japan,* **44,** 25–43.

McCreary, J. P., P. K. Kundu, and R. Molinari, 1993: A numerical investigation of dynamics, thermodynamics and mixed-layer processes in the Indian Ocean. *Prog. Oceanogr.,* **31,** 181–244.

Murtugudde, R., J. P. McCreary Jr., and A. J. Busalacchi, 2000: Oceanic processes associated with anomalous events in the Indian Ocean with relevance to 1997–1998. *J. Geophys. Res.,* **105,** 3295–3306.

Nitta, T., and S. Yamada, 1989: Recent warming of tropical sea surface temperature and its relationship to the Northern Hemisphere. *J. Meteor. Soc. Japan,* **67,** 375–383.

Parker, D. E., C. Folland, A. Scaife, J. Knight, A. Colman, P. Baines, and B. Dong, 2007: Decadal to multidecadal variability and the climate change background. *J. Geophys. Res.,* **112,** D18115, doi:10.1029/2007JD008411.

Power, S. B., T. Casey, C. Folland, A. Colman, and V. Mehta, 1999: Interdecadal modulation of the impact of ENSO on Australia. *Climate Dyn.,* **15,** 319–324.

Rao, R. R., M. S. Girishkumar, M. Ravichandran, V. V. Gopalakrishna, and P. Thadathil, 2008: Observed mini-cold pool south of Indo-Sri Lanka Channel and its intrusion into the southeastern Arabian Sea during winter. *Deep-Sea Res. I,* **55,** 1009–1020.

Rao, S. A., and S. K. Behera, 2005: Subsurface influence on SST in the tropical Indian Ocean: Structure and interannual variability. *Dyn. Atmos. Oceans,* **39,** 103–135.

Rayner, N. A., D. E. Parker, E. B. Horton, C. K. Folland, L. V. Alexander, D. P. Rowell, E. C. Kent, and A. Kaplan, 2003: Global analyses of sea surface temperature, sea ice, and night marine air temperature since the late nineteenth century. *J. Geophys. Res.,* **108,** 4407, doi:10.1029/2002JD002670.

——, P. Brohan, D. E. Parker, C. K. Folland, J. J. Kennedy, M. Vanicek, T. Ansell, and S. F. B. Tett, 2006: Improved analyses of changes and uncertainties in sea surface temperature measured in situ since the mid-nineteenth century: The HadSST2 dataset. *J. Climate,* **19,** 446–469.

Reason, C. J. C., R. J. Allan, J. A. Lindesay, and T. J. Ansell, 2000: ENSO and climatic signals across the Indian Ocean basin in the global context. Part I: Interannual composite patterns. *Int. J. Climatol.,* **20,** 1285–1327.

Schott, F. A., S.-P. Xie, and J. P. McCreary, 2009: Indian Ocean circulation and climate variability. *Rev. Geophys.,* **47,** RG1002, doi:10.1029/2007RG000245.

Shinoda, T. M., A. Alexander, and H. H. Hendon, 2004: Remote response of the Indian Ocean to interannual SST variations in the tropical Pacific. *J. Climate,* **17,** 363–372.

Smith, T. M., and R. W. Reynolds, 2004: Improved extended reconstruction of SST (1854–1997). *J. Climate,* **17,** 2466–2477.

——, R. E. Livezey, and S. S. Shen, 1998: An improved method for analyzing sparse and irregularly distributed SST data on a regular grid: The tropical Pacific Ocean. *J. Climate,* **11,** 1717–1729.

Terray, P., and S. Dominiak, 2005: Indian Ocean sea surface temperature and El Niño–Southern Oscillation: A new perspective. *J. Climate,* **18,** 1351–1368.

Thompson, D. W. J., J. J. Kennedy, J. M. Wallace, and P. D. Jones, 2008: A large discontinuity in the mid-twentieth century in observed global-mean surface temperature. *Nature,* **453,** 646–649.

Tokinaga, H., and Y. Tanimoto, 2004: Seasonal transition of SST anomalies in the tropical Indian ocean during El Niño and Indian Ocean dipole years. *J. Meteor. Soc. Japan,* **82,** 1007–1018.

Tozuka, T., T. Yokoi, and T. Yamagata, 2010: A modeling study of interannual variations of the Seychelles Dome. *J. Geophys. Res.,* **115,** C04005, doi:10.1029/2009JC005547.

Trenberth, K. E., and J. W. Hurrell, 1994: Decadal atmosphere–ocean variations in the Pacific. *Climate Dyn.,* **9,** 303–319.

Venzke, S., M. Latif, and A. Villwock, 2000: The coupled ECHO-2. Part II: Indian Ocean response to ENSO. *J. Climate,* **13,** 1371–1383.

Wang, B., and S.-I. An, 2005: A method for detecting season-dependent modes of climate variability: S-EOF analysis. *Geophys. Res. Lett.,* **32,** L15710, doi:10.1029/2005GL022709.

——, R. Wu, and X. Fu, 2000: Pacific–East Asian teleconnection: How does ENSO affect East Asian climate? *J. Climate,* **13,** 1517–1536.

——, Q. Ding, X. Fu, I.-S. Kang, K. Jin, J. Shukla, and F. Doblas-Reyes, 2005: Fundamental challenge in simulation and prediction of summer monsoon rainfall. *Geophys. Res. Lett.,* **32,** L15711, doi:10.1029/2005Gl022734.

——, J. Yang, T. J. Zhou, and B. Wang, 2008: Interdecadal changes in the major modes of Asian–Australian monsoon variability: Strengthening relationship with ENSO since late 1970s. *J. Climate,* **21,** 1771–1789.

——, and Coauthors, 2009: Advance and prospectus of seasonal prediction: Assessment of APCC/CliPAS 14-model ensemble retrospective seasonal prediction (1980–2004). *Climate Dyn.,* **33,** 93–117.

Wang, C., W. Wang, D. Wang, and Q. Wang, 2006: Interannual variability of the South China Sea associated with El Niño. *J. Geophys. Res.,* **111,** C03023, doi:10.1029/2005JC003333.

Wang, H., and V. M. Mehta, 2008: Decadal variability of the Indo-Pacific warm pool and its association with atmospheric and oceanic variability in the NCEP–NCAR and SODA reanalyses. *J. Climate,* **12,** 5545–5565.

Wang, L., W. Chen, and R. Huang, 2008: Interdecadal modulation of PDO on the impact of ENSO on the East Asian winter monsoon. *Geophys. Res. Lett.,* **35,** L20702, doi:10.1029/2008GL035287.

Watanabe, M., and F.-F. Jin, 2002: Role of Indian Ocean warming in the development of Philippine Sea anticyclone during ENSO. *Geophys. Res. Lett.,* **29,** 1478, doi:10.1029/2001GL014318.

Woodruff, S. D., and Coauthors, 2011: ICOADS release 2.5: Extensions and enhancements to the surface marine meteorological archive. *Int. J. Climatol.,* **31,** 951–967.

Wu, R., and S.-P. Xie, 2003: On equatorial Pacific surface wind changes around 1977: NCEP–NCAR reanalysis versus COADS observation. *J. Climate,* **16,** 167–173.

——, and S. W. Yeh, 2010: A further study of the tropical Indian Ocean asymmetric mode in boreal spring. *J. Geophys. Res.,* **115,** D08101, doi:10.1029/2009JD012999.

——, B. P. Kirtman, and V. Krishnamurthy, 2008: An asymmetric mode of tropical Indian Ocean rainfall variability in boreal spring. *J. Geophys. Res.,* **113,** D05104, doi:10.1029/2007JD009316.

Xie, P., and P. A. Arkin, 1997: Global precipitation: A 17-year monthly analysis based on gauge observations, satellite estimates, and numerical model outputs. *Bull. Amer. Meteor. Soc.,* **78,** 2539–2558.

Xie, S.-P., H. Annamalai, F. A. Schott, and J. P. McCreary, 2002: Structure and mechanisms of South Indian Ocean climate variability. *J. Climate,* **15,** 864–878.

——, Q. Xie, D. X. Wang, and W. T. Liu, 2003: Summer upwelling in the South China Sea and its role in regional climate variations. *J. Geophys. Res.,* **108,** 3261, doi:10.1029/2003JC001867.

——, K. Hu, J. Hafner, H. Tokinaga, Y. Du, G. Huang, and T. Sampe, 2009: Indian Ocean capacitor effect on Indo-western Pacific climate during the summer following El Niño. *J. Climate,* **22,** 730–747.

——, Y. Du, G. Huang, X.-T. Zheng, H. Tokinaga, K. Hu, and Q. Liu, 2010: Decadal shift in El Niño influences on Indo–western Pacific and East Asian climate in the 1970s. *J. Climate,* **23,** 3352–3368.

Yang, J., Q. Liu, S.-P. Xie, Z. Liu, and L. Wu, 2007: Impact of the Indian Ocean SST basin mode on the Asian summer monsoon. *Geophys. Res. Lett.,* **34,** L02708, doi:10.1029/2006GL028571.

Yu, L., and M. M. Rienecker, 1999: Mechanisms for the Indian Ocean warming during the 1997–98 El Niño. *Geophys. Res. Lett.,* **26,** 735–738.

Zheng, X.-T., S.-P. Xie, and Q. Liu, 2011: Response of the Indian Ocean basin mode and its capacitor effect to global warming. *J. Climate,* **24,** 6146–6164.